TRIBHUVAN UNIVERSITY
INSTITUTE OF ENGINEERING
PULCHOWK CAMPUS

THESIS NO: M-19-MSMDE-2018/2020

Aeroelastic Energy Harvesting: A Case for Galloping

by

Sandip Thakur

A THESIS
SUBMITTED TO
THE DEPARTMENT OF MECHANICAL AND AEROSPACE ENGINEERING
IN PARTIAL FULFILLMENT OF THE REQUIREMENTS FOR THE
DEGREE OF MASTER OF SCIENCE IN
MECHANICAL SYSTEMS DESIGN AND ENGINEERING

DEPARTMENT OF MECHANICAL ENGINEERING
LALITPUR, NEPAL

JULY, 2020

COPYRIGHT

TRIBHUVAN UNIVERSITY
INSTITUTE OF ENGINEERING
PULCHOWK CAMPUS
DEPARTMENT OF MECHANICAL AND AEROSPACE ENGINEERING

The undersigned certify that they have read and recommended to the Institute of Engineering for acceptance, a thesis entitled **"Aeroelastic Energy Harvesting: A Case for Galloping "** submitted by Sandip Thakur in partial fulfillment of the requirements for the Degree of Master of Science in Mechanical Systems Design and Engineering.

_____

Supervisor, Laxman Poudel, Ph.D.
Professor
Department of Mechanical and Aerospace Engineering

_____

Supervisor, Kamal Darlami
Assistant Professor
Department of Mechanical and Aerospace Engineering

_____

External Examiner, Dr. Sailesh Chitrakar
Lecturer
Department of Mechanical Engineering
Kathmandu University, Dhulikhel, Kavre

_____

Committee Chairperson, Nawraj Bhattarai, Ph.D.
Head of Department
Department of Mechanical and Aerospace Engineering

_____

Date

ABSTRACT

Energy Harvesting (EH) from transverse galloping of bluff bodies can be used to convert wind energy into electrical power to develop self-powered devices (like sensors). This paper focuses on the numerical investigation of flow-induced vibration based energy harvesting by the use of piezoelectric material. Different turbulence models are analyzed for the CFD simulations of which the Realizable k-ϵ model yielded the most accurate solution. Two way coupled fluid-structure interaction simulation is carried out to get the displacement of a square base prism and the result is used to calculate the power produced. A maximum power output of $2.1\ mW$ is predicted at a wind velocity of $12\ m/s$.

ACKNOWLEDGEMENTS

First of all, I would like to express my sincerest gratitude to my supervisors, Prof. Dr. Laxman Poudel and Asst. Prof. Kamal Darlami, Department of Mechanical and Aerospace Engineering, Pulchowk Campus for continuously guiding me in the course of my thesis work. They have tirelessly helped me in every step of the way and their positive outlook on any research process has changed my outlook on research into something that should be done passionately but at an easy pace.

Secondly, I would like to thank Asst. Prof. Hari Dura, Department of Mechanical and Aerospace Engineering, Pulchowk Campus for providing me with important insights into simulations and also providing me with the computational resources.

Furthermore, I would like to express my deepest gratitude to Asst. Prof. Manoj Paudel, Nepal Engineering College, Bhaktapur for always maintaining the appropriate level of motivation and humor during the trying times.

I would also like to thank the entire Department of Mechanical and Aerospace Engineering, Pulchowk Campus, for their support in the completion of this work.

Moreover, I would like to thank Er. Hemanta Dulal, Er. Rojesh Shikhrakar and Er. Saleen Bhattarai for their help and support during research work.

Lastly and most importantly, I would like to thank my beloved family; my mother Mrs. Renu Devi, my father Mr. Mahatam Thakur and my sisters Nitu and Punam for their continuous support and motivation. I would not be here today without them.

TABLE OF CONTENTS

LIST OF TABLES

LIST OF FIGURES

LIST OF SYMBOLS

M_{tip} , L_{tip}	Mass and length of the tip body
U_i	Onset speed
P	Harvested power
U_{rel}	Relative velocity
α	Angle of attack
F_y	Vertical force component
C_y	Vertical force coefficient
ζ	Mechanical damping ratio
ζ_T	Net damping factor
U_{crit}	Critical velocity
ω_N	Natural circular frequency of oscillations
C_L	Lift coefficient
C_D	Drag Coefficient
C_p	Equivalent capacitance of piezoelectric sheets
θ	Electromechanical coupling term
R_L	Electrical load resistance
V	Harvested voltage
k	Turbulent kinetic energy
ϵ	Turbulence dissipation rate
δ	Strain components
y^+	Y plus value
St	Strouhal number
Re	Reynolds number

LIST OF ABBREVIATIONS

CAD	Computer Aided Drawing
CFD	Computational Fluid Dynamics
CFL	Courant–Friedrichs–Lewy
CSM	Computational Structural Mechanics
DNS	Direct Numerical Simulation
EH	Smoothed Particle Hydrodynamics
FSI	Fluid Structure Interaction
IB	Immersed Boundary
IoTs	Internet of Things
LB	Lattice Boltzmann
LES	Large Eddy Simulation
MATLAB	Matrix Laboratory
MEMS	Micro Electromechanical Systems
N-S	Navier-Stokes
RANS	Reynolds-Averaged Navier-Stokes
RKE	Realizable $k-\epsilon$
SKE	Standard $k-\epsilon$
TG	Transverse Galloping
VIV	Vortex Induced Vibration

CHAPTER ONE : INTRODUCTION

1.1. Background

Energy harvesting (EH) is the process of extracting the minute amount of energy (light, thermal, or kinetic energy) from the ambient energy sources which can be used to develop self-powered devices like sensors, Micro Electromechanical Systems (MEMS) or actuators, and other devices through the use of electromagnetic, electrostatic or piezoelectric transduction mechanisms. As the piezoelectric transducer operates extensively to the wide range of frequencies, this mechanism is preferred mostly to develop efficient and simple EH devices (Abdelkefi, 2016).

When a structure is directed to flow loads, unwanted and excessive vibrations like vortex-induced vibrations (VIV), flutter and galloping are induced due to aerodynamic phenomenon. So, when the energy harvester is subjected to a flow field and perturbed to go large oscillations then electrical energy can be extracted based on flutter, vortex-induced vibrations or galloping.

Table 1-1: Comparisons between various aeroelastic EH

	Design	M_{tip} **(kg)**	L_{tip} (cm)	U_i **(m/s)**	**PZT type**	**No. of Layers**	**P (mW)**
Flutter (Bryant and Garcia, 2011)	NACA 0012	0.00966	13.6	1.9	Quick pack QP 10N	2 parallel	2.2
Flutter (Abdelkefi and Hajj, 2013)	Symmetric	1.06	60	10.9	PSI-5A4E	1	0.2
VIV (Akaydin et al., 2010)	Circular	2.32	122	7.3	PVDF	1	0.004
VIV (Akaydin et al., 2012)	Circular	0.016	20.3	1.2	PZT-5A	2 series	0.1
Galloping (Sirohi and Mahadik, 2012)	D-section	0.024	25.1	3.57	PSI-5H4E	2 parallel	1.14
Galloping Zhao, Tang, and Yang (2013)	Square	0.026	15	2.5	DuraAct P876A12	2 parallel	8.4

	Design	M_{tip} (kg)	L_{tip} (cm)	U_i (m/s)	PZT type	No. of Layers	P (mW)
Galloping Bibo, Abdelkefi, and Daqaq (2015)	Square	0.102	10.6	2.3	MFC-M8514-P2	1	0.22

(Source: Abdelkefi, 2016)

Here, M_{tip} represents the tip mass, L_{tip} depicts the length of the tip body, U_i is the onset speed of corresponding vibrations, and P is the maximum harvested power.

From the Quantitative comparison made by Abdelkefi, (2016), it is clear that galloping based energy harvester is the most efficient and can harvest higher power compared to other flow-induced energy harvester. So, galloping based energy harvesting is focused in this study.

Galloping can be defined as a velocity dependent, damping-controlled instability, inducing transverse motion having a low frequency, and large-amplitude in the direction normal to the flow field. A. Barrero-Gil et al., (2010) analyzed theoretically the feasibility of using a transverse galloping phenomenon to extract energy from a fluid flow when elastic bluff bodies are exposed to the incident flow having velocity greater than the certain critical value.

1.2. Research Gap

In galloping, the major limitation is the characterization of the aerodynamic loads in galloping phenomenon. Although the quasi-steady approximation is considered in previous studies (Abdelkefi, 2016), proper development of unsteady representation is required to determine the galloping force. Also, proper determination of the linear and nonlinear coefficients is required for the representation of galloping force. Numerical and experimental researches (Barrero-Gil, Alonso and Sanz-Andres, 2010), (Zhao, Tang and Yang, 2013) and (Bibo, Abdelkefi and Daqaq, 2015) have been done to determine these coefficients for a square cross-section but these coefficients are different due to various characterization techniques used by them, also they have considered it for different ranges of Reynolds number. So, proper representation of these coefficients is required for different cross-sections and definite ranges of Reynolds number. Therefore, a better approximation of the parameters of the system

can be carried out. Also, a better investigation is required for determination of the effects of nonlinearities on the performance of the harvester.

1.3. Objectives

1.3.1. Main Objective

- The main objective of this research is the numerical investigation of flow-induced vibration based energy harvesting.

1.3.2. Specific Objectives

The specific objectives in order to meet the main objectives are as follows:

- To perform CFD simulations and analysis of different numerical techniques.
- To carry out two-way coupled Fluid-Structure Interaction simulation to get the displacement of a square base prism.
- To predict the amount of energy that could be harvested from the galloping phenomenon by the use of piezoelectric material.
- To account the geometric nonlinearities of piezoelectric material with a numerical scheme.

1.4. Scope and Limitations of Work

Energy harvesting (EH) is a potential technology that will replace batteries within the near future. It extracts energy from ambient sources which can be converted to usable electric energy using various transduction mechanisms. Suitable and significant transducers for various applications can be harvested, stored to operate self-powered sensors and recharging onboard batteries. On the entire, with the present rapid enhancement of the Internet of Things (IoTs), energy harvesting provides significant merits and opportunities for developing and implementing for smart cities, homes, smart agriculture, industry, and so on. Along with this, it can be promising for creating an enhanced type of autonomous self-powered terminals which will operate for much longer periods. Thus, it can reduce the need for battery charges. Furthermore, it can also reduce costs by significantly retarding battery replacement and increasing the robustness in all its applications.

In order to simplify the analysis process and accelerate the computational times, only incompressible flow is considered in light of the available computing resources. Although the quasi-steady approximation is considered in the research, proper development of unsteady flow representation is required for higher velocities in order to determine the galloping force.

Considering the experimental constraints of wind tunnel available in Pulchowk Campus, Institute of Engineering (IOE) whose maximum achievable velocity is $12\ m/s$, velocity inlet of $12\ m/s$ is applied in x-direction.

CHAPTER TWO : LITERATURE REVIEW

The field of EH has become a focal research topic in the last decade with the ultimate aim of developing self-powered sensors, Micro Electromechanical Systems (MEMS) or actuators, and other devices that can harness energy from o ambient sources.

Den Hartog, (1956) for the first time in 1943, studied and explained the galloping phenomenon. He proposed the quasi-steady hypothesis for the representation of galloping aerodynamic loads and introduced a criterion for instability of a structure due to galloping. Generally, when the elastic bluff bodies are exposed to wind loads then transverse galloping occurs when the flow speed is greater than the critical value and then the bluff body starts to oscillate.

Barrero-Gil, Alonso and Sanz-Andres, (2010) analyzed transverse galloping (TG) possibilities for energy harvesting theoretically.

Sirohi and Mahadik, (2012) investigated wind EH from transverse galloping of a D-shaped cross-section in which they used a cantilever beam attached to the tip body and bonded with two piezoelectric sheets. They stated the increase in wind speed, increases the power output significantly. Also, they determined that a critical speed of 5.6 mph is needed for harvesting energy and at a wind speed of 10.5 mph, the maximum harvested power of 1.14 mW is obtained.

Sirohi and Mahadik, (2011) studied EH from galloping of an equilateral triangle section which is attached to cantilever beam bonded with four piezoelectric sheets. Their device produced maximum power of 50 mW at a flow speed of 11.6 mph that can be used to power various sensors.

Abdelkefi, Nayfeh and Hajj, (2012) investigated EH from galloping of square cylinder accounting the Reynolds number effect on harvested power. They found that the Reynolds number and the electrical load resistance across piezoelectric greatly affect the amount of energy harvested.

Abdelkefi, Yan and Hajj, (2013) developed a galloping based nonlinear model for piezoelectric EH which was compared with the corresponding results of Sirohi and Mahadik, (2011).

Abdelkefi, Hajj and Nayfeh, (2013), Abdelkefi, Yan and Hajj, (2013)) analyzed theoretically the effects of various cross-section geometry. The critical speed and the maximum power was compared for various cross-sections (D-section, triangles, square, and rectangles). They found that the isosceles triangle with $\delta = 30^0$ and the square cross-sections harvested maximum amount of energy at low speeds whereas, at high flow speeds, the D-section harvested the maximum amount of energy.

Also, Yang, Zhao and Tang, (2013) experimented the effect of the cross-section geometry, compared and validated the lumped parameter model coefficients with the experimental results. They found the square geometry best in comparison to other cross-sections. They determined a power output of 8.4 mW.

Abdelkefi, Yan and Hajj, (2013) carried out nonlinear characterization of the Energy harvester which is attached to the vibratory base excitations and subjected to the aerodynamic loading. They used different sections like power spectra, phase portraits, and Poincare sections for analyzing nonlinear dynamics.

Quasi-steady approximation is been considered in previous studies for energy harvesting based on galloping phenomenon.

2.1. Physical Mechanism of Galloping

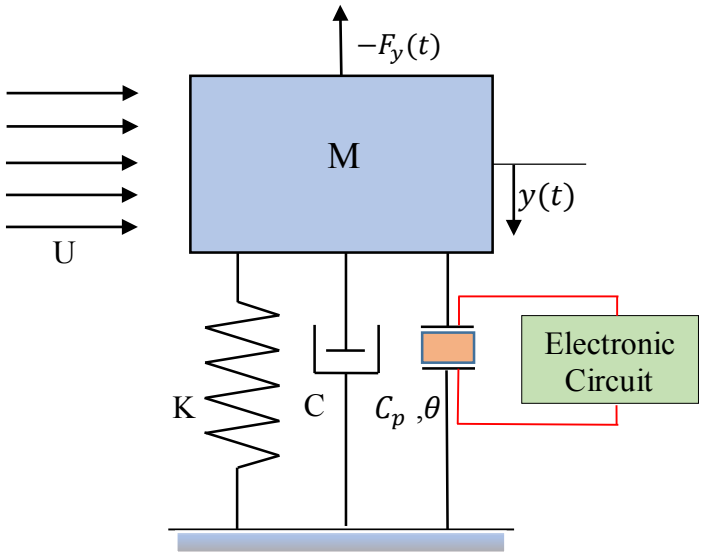

(Blevins, 2001)

Figure 2-1: Physical mechanism of galloping model.

Figure (2-1) shows a spring supported model which is subjected to a flow loads having velocity, U, density, ρ and the stiffness of spring per unit length (K). The steady aerodynamic forces i.e. the lift force and the drag force acting on the model are given as,

$$F_D = \frac{1}{2}\rho U_{rel}^2 D C_D \qquad F_L = \frac{1}{2}\rho U_{rel}^2 D C_L \qquad \text{Eq. 2.1}$$

where, the width D is used to non-dimensionalize the lift and drag aerodynamic coefficients C_L and C_D.

A Quasi-steady approximation is used to analyze the stability of the model.

When the model moves downward, the angle of attack relative to the flow is

$$\alpha = \tan^{-1}\left(\frac{\dot{y}}{U}\right) \qquad \text{Eq. 2.2}$$

where, α is the angle of attack.

Here, $\alpha = 0$ is used as a reference to the equilibrium position, $y = 0$. The downward vertical displacement is taken as positive y. The relative fluid velocity of which is the sum of the flow velocity and the induced velocity is given as,

$$U_{rel}^2 = \dot{y}^2 + U^2 \qquad \text{Eq. 2.3}$$

where, $\dot{y} = \frac{dy}{dt}$ is the vertical velocity, F_y is the resultant vector of lift and drag in the vertical plane, which is positive in downward,

$$F_y = -F_L cos\alpha - F_D sin\alpha = \frac{1}{2}\rho U^2 D C_y \qquad \text{Eq. 2.4}$$

where, the vertical force coefficient is,

$$C_y = -\frac{U_{rel}^2}{U^2}(C_L cos\alpha + C_D sin\alpha) \qquad \text{Eq. 2.5}$$

For small angles of attack, α, U_{rel} and C_y can be expanded in power

$$\alpha = \frac{\dot{y}}{U} + O(\alpha^2)$$

$$U_{rel} = U + O(\alpha^2)$$

$$\begin{aligned} C_y(\alpha) &= \mathrm{C_y}|_{\alpha=0} + \frac{\partial C_y}{\partial \alpha}|_{\alpha=0}\,\alpha + O(\alpha^2) \\ &= -C_L|_{\alpha=0} - \left[\frac{\partial C_L}{\partial \alpha} + C_D\right]_{\alpha=0}\alpha + O(\alpha^2) \end{aligned} \qquad \text{Eq. 2.6}$$

where, $O(\alpha^2)$ is the term which is proportional to α^2 and higher powers of α have been neglected. Also, the slope of the vertical force at $\alpha = 0$ is

$$\frac{\partial C_y}{\partial \alpha}|_{\alpha=0} = -\left(\frac{\partial C_L}{\partial \alpha} + C_D\right)_{\alpha=0} \qquad \text{Eq. 2.7}$$

At zero angle of attack ($\alpha = 0$), $C_y = -C_L$.

The equation of motion representing the spring-supported, and damped model responding to the aerodynamic force is given by Equation (2.8).

$$m(\ddot{y}) + 2\zeta\omega_N\dot{y} + \omega_N^2 y) = F_y = \frac{1}{2}\rho U^2 D C_y \qquad \text{Eq. 2.8}$$

where, m is the mass per unit length, ζ is the mechanical damping ratio and ω_N is the natural circular frequency of oscillations. Neglecting higher orders of α, we have

$$m\left(\ddot{y}\right) + 2\omega_N \left(\zeta - \frac{\rho U D}{4m\omega_N}\frac{\partial C_y}{\partial \alpha}|_{\alpha=0}\right)\dot{y} + \omega_N^2 y\Big) = -\frac{1}{2}\rho U^2 D C_L|_{\alpha=0} \qquad \text{Eq. 2.9}$$

$$\omega_N = 2\pi f = (k/m)^{1/2}$$

$$\zeta_T = \zeta - \frac{\rho U D}{4m\omega_N}\frac{\partial C_y}{\partial \alpha}|_{\alpha=0}$$

(Paidoussis et al., 2011)

where, ζ_T is the net damping factor which is the equivalent of aerodynamic and structural components.

When the net damping of the system becomes negative then unstable oscillations, i.e., galloping, will occur. Thus, the model will be unstable if $\frac{\partial C_y}{\partial \alpha} > 0$ or equivalently $\frac{\partial C_L}{\partial \alpha} + C_D < 0$ which is called as Den Hartog, (1956) criterion and which is used to predict the occurrence of galloping on any given structure.

U_{crit} is the critical velocity for the onset of galloping instability which can be determined by setting ζ_T to zero.

$$U_{crit} = \left(\frac{4m\omega_N\zeta}{\rho D}\right)\Big/\left(\frac{\partial C_y}{\partial \alpha}\right) \qquad \text{Eq. 2.10}$$

2.2. Electromechanical model representation

A simplified spring supported, damped elastic bluff body configuration susceptible to galloping in the transverse direction is considered which is subjected to the incoming flow shown in Figure 2-1). The governing equation of the system having piezoelectric transducer with a resistive load across the electrical circuit is given as,

$$m(\ddot{y} + 2\zeta\omega_N\dot{y} + \omega_N^2 y) - \frac{\theta}{l}V = F_y = \frac{1}{2}\rho U^2 D C_y$$

$$C_p\dot{V} + \frac{V}{R} + \theta\dot{y} = 0 \qquad \text{Eq. 2.11}$$

(Abdelkefi, Hajj and Nayfeh, 2013)

where, l is the structure's length, θ is the electromechanical coupling term, V is the harvested, R is the load resistance across piezoelectric, C_p is the equivalent capacitance of the piezoelectric sheets, F_y is the vertical fluid force per unit length in the transverse direction normal to the incident flow, and C_y is the vertical force coefficient. The differentiation with respect to time 't' is represented by the dot symbols.

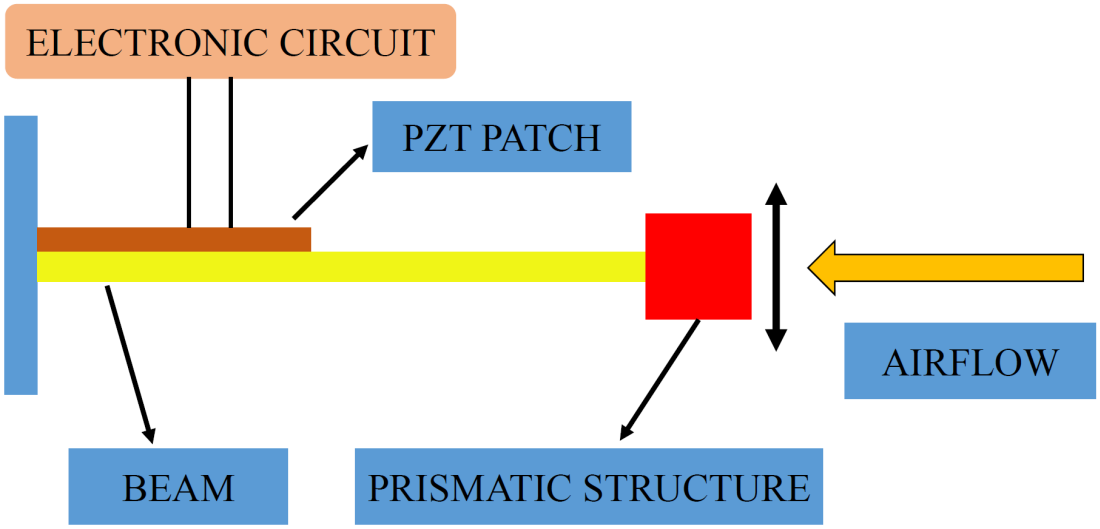

(Elahi, Eugeni and Gaudenzi, 2018)

Figure 2-2: Schematic diagram of galloping based energy harvester

When the timescale of the oscillating bluff body ($\sim 2\pi/\omega_N$) is substantially greater than the time scale of the fluid flow (~D/U) then the transverse galloping phenomenon can be analyzed using the quasi-steady hypothesis.

2.2.1. Linear analysis:

The effects of the load resistance, damping of the energy harvester and linear analysis of the system for galloping can be analyzed as,

$$\mathbf{X}=\begin{bmatrix} X_1 \\ X_2 \\ X_3 \end{bmatrix} = \begin{bmatrix} y \\ \dot{y} \\ V \end{bmatrix}$$

$$\dot{X}_1 = X_2$$

$$\dot{X}_2 = -\left(2\zeta\omega_N - \frac{\rho U D a_1}{2m}\right) X_2 - \omega_N^2 X_1 + \frac{\theta}{m} X_3 + \frac{\rho D a_3}{2mU} X_2^3$$

$$\dot{X}_3 = -\frac{1}{RC_p} X_3 - \frac{\theta}{C_p} X_2 \qquad \text{Eq. 2.12}$$

These equations are in the form

$\dot{\boldsymbol{X}} = D\boldsymbol{X} + \mathbf{A(X, X, X)}$

$$D = \begin{bmatrix} 0 & 1 & 0 \\ -\omega_N^2 & -\left(2\zeta\omega_N - \frac{\rho U D a_1}{2m}\right) & \frac{\theta}{m} \\ 0 & -\frac{\theta}{C_p} & -\frac{1}{RC_p} \end{bmatrix}$$

where, D is the matrix that incorporates all the parameters affecting the system and **A(X, X, X)** is the cubic vector function.

2.3. System coupling

Fluid-structure Interaction (FSI*)* is a coupling of Computational Fluid Dynamics (CFD) and Computational Structural Mechanics (CSM) in which the information is exchanged at the interface between Fluid and Structural numerical solvers, which is known as the system coupling. It is further classified as two types.

2.3.1. One-way coupling

In one-way coupling, the fluid pressure acting at the interface of the structure is transferred to the structural solver but the displacement reaction of a structure on a fluid field is negligible.

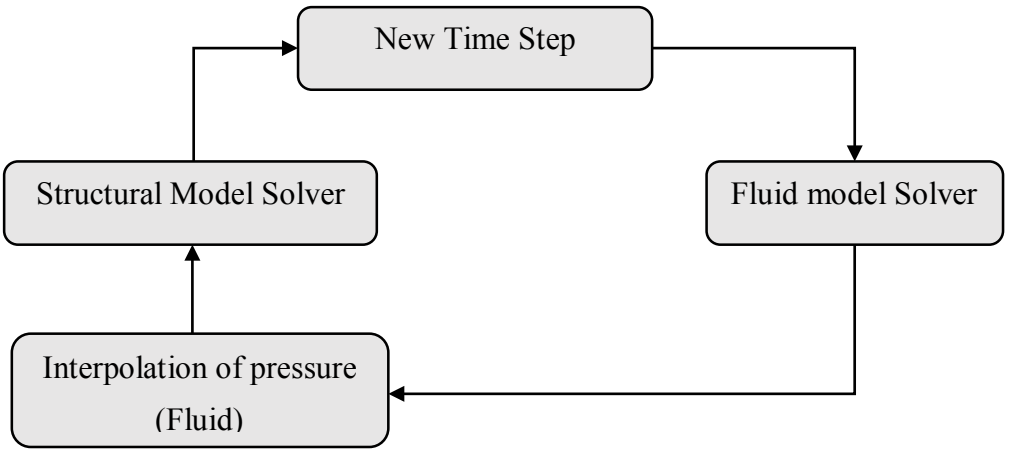

Figure 2-3: One way coupling flow chart (Raja, 2012)

2.3.2. Two-way coupling

Two-way coupling is significant where the motion of fluid greatly affects the solid structure and also the fluid field is also affected by the reaction of a solid structure at the same time (Benra *et al*., 2011). In these calculations, along with the transfer of fluid pressure to the structure model solver, the reaction of the structure (i.e. displacement) is also transferred to the fluid model solver.

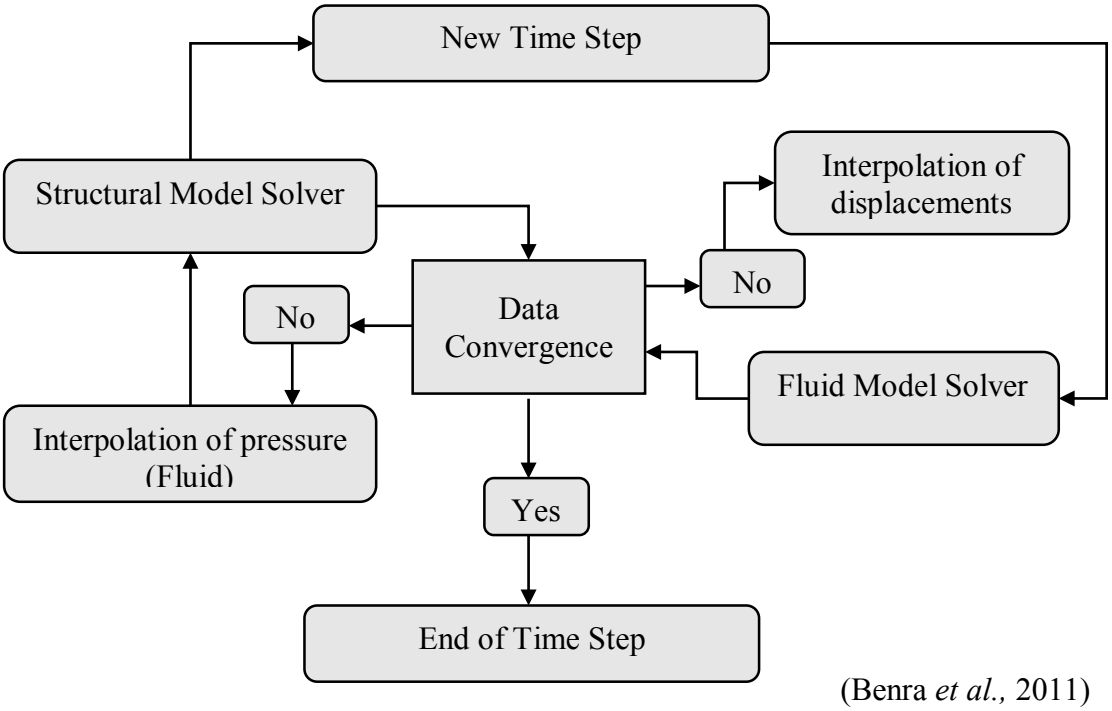

(Benra *et al.,* 2011)

Figure 2-4: Two-way coupling flow chart

2.4. Turbulence Modelling

2.4.1. Large Eddy Simulation (LES) Model

LES model explicitly resolves the large eddies and implicitly account the small eddies using subgrid-scale model (Ochoa and Fueyó, 2004). LES model lies in-between DNS and RANS on the basis of the fraction of the resolved scales (ANSYS Inc, 2013). The theory explaining LES model is listed as follows:

- Large eddies mostly transport momentum, mass, energy, and other passive scalars.
- Large eddies are greatly dependent on the geometries and boundary conditions of the flow.
- Small eddies are consequently more universal as they are more isotropic and less dependent on the geometry.

2.4.1.1. Filtered Navier-Stokes Equations

Fourier space or configuration space in the time-dependent Navier-Stokes equations is filtered to obtain the governing equations for LES model. The scale of eddies smaller than the filter width are filtered using the filtering process and then the obtained resulting equation governs the dynamics of large eddies.

A filtered variable is represented as,

$$\overline{\phi}(x) = \int_D \phi\,(x')G(x,x')dx'$$

where, G is the filter function and D is the fluid domain.

The finite-volume discretization in ANSYS FLUENT gives the filtering operation implicitly as:

$$\overline{\phi}(x) = \frac{1}{\mathrm{V}}\int_D \phi\,(x')dx'\,, x'\epsilon\,\nu$$

where, V is the volume of a computational cell.

The filter function, $\boldsymbol{G(x,x')}$, is given as,

$$G(x,x') = f(x) = \begin{cases} \frac{1}{V}\,, & x'\epsilon\,\nu \\ 0\,, & x'\ otherwise \end{cases}$$

Although the theory represented here is for incompressible flows, the LES in ANSYS FLUENT can also be applied to compressible flows.

Filtering the Navier-Stokes equations, one obtains

$$\frac{\partial \rho}{\partial t} + \frac{\partial(\rho\overline{u_\iota})}{\partial x_i} = 0$$

$$\frac{\partial}{\partial t}(\rho\overline{u_\iota}) + \frac{\partial}{\partial x_j}\left(\rho\overline{u_\iota}\,\overline{u_J}\right) = \frac{\partial}{\partial x_j}(\sigma_{ij}) - \frac{\partial \bar{p}}{\partial x_i} - \frac{\partial \tau_{ij}}{\partial x_j} \qquad \text{Eq. 2.13}$$

Where, σ_{ij} is the stress tensor due to molecular viscosity which can be defined as,

$$\sigma_{ij} \equiv \left[\mu\left(\frac{\partial(\overline{u_\iota})}{\partial x_j} + \frac{\partial\left(\overline{u_J}\right)}{\partial x_i}\right)\right] - 2/3\mu\frac{\partial(\overline{u_l})}{\partial x_l}\delta_{ij}$$

And τ_{ij} is the subgrid-scale stress represented by

$$\tau_{ij} \equiv \rho\overline{u_\iota u_J} - \rho\overline{u_\iota}\,\overline{u_J}$$

2.4.1.2. Smagorinsky Closure

Smagorinsky proposed this model in 1963 (Smagorinsky, 1963) and it is commonly employed nowadays. Similar with the consequences of stress in laminar flows, the subgrid-scale can be represented as:

$$\tau_{ij} - \frac{1}{3}\tau_{kk}\delta_{ij} = -2\nu_T \overline{S_{ij}}$$

where ν_T is the eddy viscosity, and $\overline{S_{ij}}$ represents the strain rate within the resolved velocity field defined as:

$$\overline{S_{ij}} = \frac{1}{2}\left(\frac{\partial(\overline{u_i})}{\partial x_j} + \frac{\partial(\overline{u_j})}{\partial x_i}\right)$$

$$\nu_T = (C_s\Delta)^2|\bar{S}|$$

where, $|\bar{S}| = \left(2\,\overline{S_{ij}}\;\overline{S_{ij}}\right)^{\frac{1}{2}}$; Δ is the associated length with the filter defined as $\Delta = \left(\Delta_x\Delta_y\Delta_z\right)^{\frac{1}{3}}$. The term C_s is a parameter which is assigned 0.2 for isotropic turbulence.

2.4.2. K – Epsilon (ϵ) Model

The $k-\epsilon$ model is a two equation based turbulence model which includes two extra transport equations i.e. one for turbulent kinetic energy (k) and another for turbulence dissipation rate (ϵ)) to represent the turbulent properties of the flow.

2.4.2.1. Standard $k-\epsilon$ (SKE) Model

The transport equations for k and ϵ in the standard $k-\epsilon$ model are

$$\frac{\partial}{\partial t}(\rho k) + \frac{\partial}{\partial x_i}(\rho k u_i) = \frac{\partial}{\partial x_j}\left[\left(\mu + \frac{\mu_t}{\sigma_k}\right)\frac{\partial k}{\partial x_j}\right] + G_k + G_b - \rho\epsilon - Y_M + S_k$$

$$\frac{\partial}{\partial t}(\rho\epsilon) + \frac{\partial}{\partial x_i}(\rho\epsilon u_i) = \frac{\partial}{\partial x_j}\left[\left(\mu + \frac{\mu_t}{\sigma_\epsilon}\right)\frac{\partial \epsilon}{\partial x_j}\right] + C_{1\epsilon}\frac{\epsilon}{k}(G_k + C_{3\epsilon}G_{b)} - C_{2\epsilon}\rho\frac{\epsilon^2}{k} + S_\epsilon$$

Eq. 2.14

(ANSYS Inc, 2013)

where, G_k represents the generation of turbulence kinetic energy due to the mean velocity gradients, G_b is the generation of turbulence kinetic energy due to buoyancy, Y_M depicts the contribution of the fluctuating dilatation, σ_k and σ_ϵ are the turbulent Prandtl numbers for k and ϵ, respectively. S_k and S_ϵ are user-defined source terms. $C_{1\epsilon}$, $C_{2\epsilon}$, $C_{3\epsilon}$ and C_μ are constants.

The model constants have the following values.

$C_{1\epsilon} = 1.44$, $C_{2\epsilon} = 1.92$, $C_\mu = 0.09$, $\sigma_k = 1$ and $\sigma_\epsilon = 1.3$

2.4.2.2. Realizable $k-\epsilon$ (RKE) Model

The realizable $k-\epsilon$ model varies with the standard $k-\epsilon$ model in the following ways:

- This model formulates turbulent viscosity in a different way.
- From an exact equation, a new transport equation has been formulated for the dissipation rate for addressing the mean-square vorticity fluctuation.

The transport equations for k and ϵ in the realizable $k-\epsilon$ model are

$$\frac{\partial}{\partial t}(\rho k) + \frac{\partial}{\partial x_j}(\rho k u_j) = \frac{\partial}{\partial x_j}\left[\left(\mu + \frac{\mu_t}{\sigma_k}\right)\frac{\partial k}{\partial x_j}\right] + G_k + G_b - \rho\epsilon - Y_M + S_k$$

$$\frac{\partial}{\partial t}(\rho\epsilon) + \frac{\partial}{\partial x_j}(\rho\epsilon u_j) = \frac{\partial}{\partial x_j}\left[\left(\mu + \frac{\mu_t}{\sigma_\epsilon}\right)\frac{\partial \epsilon}{\partial x_j}\right] + C_{1\epsilon}\frac{\epsilon}{k}C_{3\epsilon}G_b + \rho C_1 S_\epsilon - \frac{C_2\rho\epsilon^2}{k+\sqrt{\nu\epsilon}} + S_\epsilon$$

Eq. 2.15

where, $C_l = max\left[0.43, \frac{\eta}{\eta+5}\right]$, $\eta = S\frac{k}{\epsilon}$, $S = \sqrt{2S_{ij}S_{ij}}$

(ANSYS Inc, 2013)

2.4.2.3. RNG $k-\epsilon$ Model

The RNG $k-\epsilon$ model employs a rigorous statistical technique (called renormalization group theory). It is analogous to the standard $k-\epsilon$ model, but has the following differences:

- This model has an additional term in its ϵ equation which is significantly accurate for extremely strained flows.
- This model also enhances the accuracy of swirling flows as it incorporates the swirling effect of flow.

- This theory uses an analytical formula for turbulent Prandtl numbers.

The transport equations for k and ϵ in the RNG $k-\epsilon$ model are

$$\frac{\partial}{\partial t}(\rho k)+\frac{\partial}{\partial x_i}(\rho k u_i)=\frac{\partial}{\partial x_j}\left[\alpha_k \mu_{eff}\frac{\partial k}{\partial x_j}\right]+G_k+G_b-\rho\epsilon-Y_M+S_k$$

$$\frac{\partial}{\partial t}(\rho \epsilon)+\frac{\partial}{\partial x_i}(\rho \epsilon u_i)=\frac{\partial}{\partial x_j}\left[\alpha_\epsilon \mu_{eff}\frac{\partial \epsilon}{\partial x_j}\right]+C_{1\epsilon}\frac{\epsilon}{k}(G_k+C_{3\epsilon}G_{b)}-C_{2\epsilon}\rho\frac{\epsilon^2}{k}-R_\epsilon+S_\epsilon$$

Eq. 2.16

(ANSYS Inc, 2013)

where, the quantities α_k and α_ϵ are the inverse effective Prandtl numbers for k and ϵ

The model constants derived analytically are found to be $C_{1\epsilon}=1.42$, $C_{2\epsilon}=1.68$

CHAPTER THREE : RESEARCH METHODOLOGY

The success of any research is always determined by the strength and relevance of the methodology used to address the research problem. Hence, it is essential to elaborate the methodological stance followed in the research.

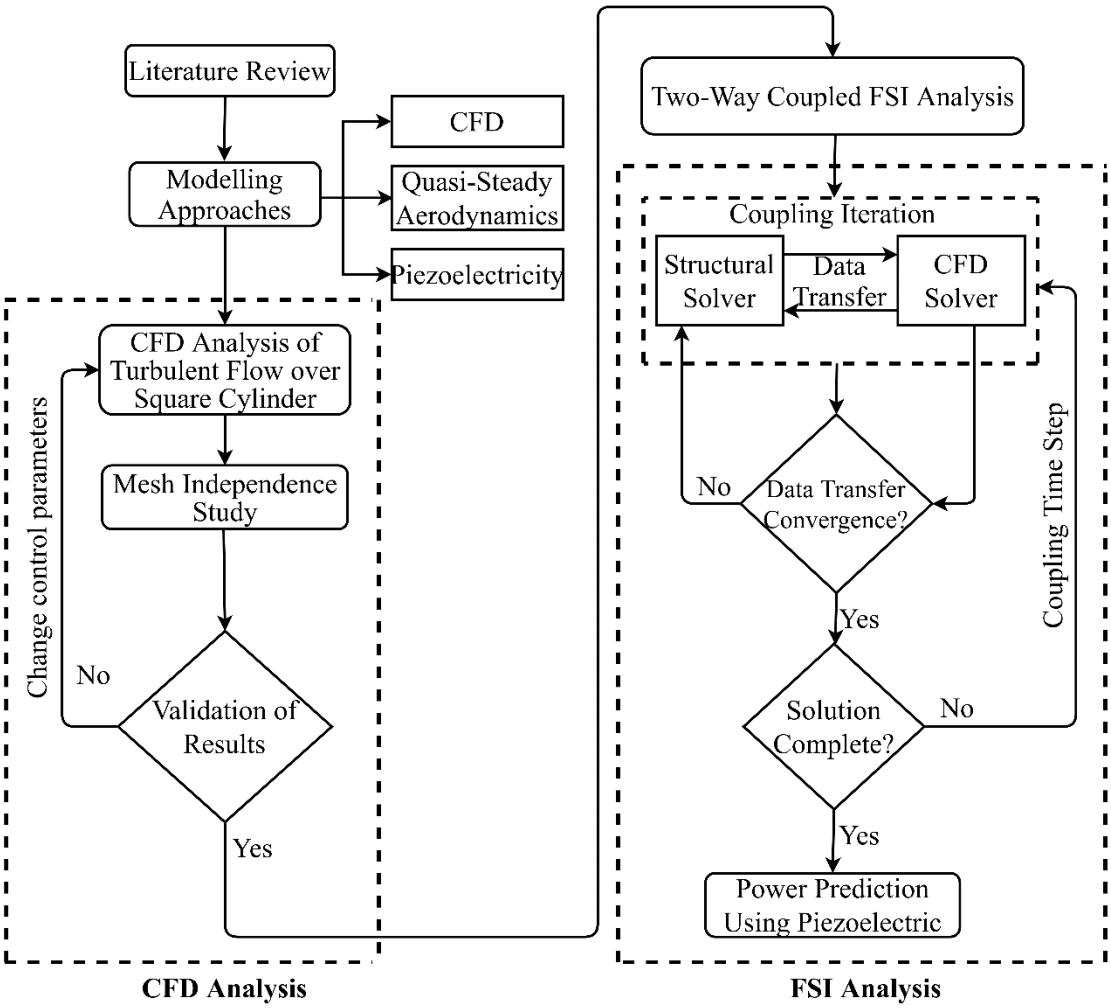

Figure 3-1: Flow diagram of Methodology

The CFD analysis of turbulent flow over square cylinder is carried out and after the validation of model, it is further used for the two-way coupled FSI analysis in which the structural solver and CFD solver are coupled. After the completion of solution, the tip displacement result is used for the power prediction using piezoelectric.

3.1. Modeling approaches

There are two main coupling parameters that are required to be accounted in the modeling of coupled aero-electro-elastic energy harvester model, aero-elastic and electro-elastic coupling. Modeling and simulation of EH system involves numerous physical phenomena from different disciplines. The interconnecting relation between these disciplines is not obvious, and hence complications may arise from the nonlinear coupling which needs to be addressed for adequate designing and optimization of the performance of EH systems. The aeroelastic equation for aerodynamic modeling and electro-elastic coupling for the piezoelectric effect is explained in the following sections:

3.1.1. Computational fluid dynamics

The Navier-Stokes equations governs the fluid flow. This governing equation can be written as,

$$\frac{\partial \rho}{\partial t} + \Delta.\left(\rho\, \vec{V}\right) = 0$$

$$\frac{\partial}{\partial t}\left(\rho\, \vec{V}\right) + \Delta.\left(\rho\, \vec{V}\, \vec{V}\right) = -\Delta P + \Delta.\left(\vec{\tau}\right) + \rho\, \vec{g} + \vec{F} \qquad \text{Eq. 3.1}$$

where, $\vec{\tau}$ is the stress vector, P is the static pressure, and $\rho\, \vec{g}$, $\vec{F}$ are the gravitational body force and the external forces.

The stress tensor vector is given by

$$\vec{\tau} = \mu\left[\left(\Delta\, \vec{V} + \Delta\, \vec{V}^{T}\right) - \frac{2}{3}\Delta\,.\vec{V}I\right]$$

where, μ is the molecular viscosity, and I is the unit tensor.

The discretization of these governing equations are generally done in either finite element, finite volume, or finite difference approach. These types of discretization techniques are applicable to most of the physical problems but the analysis of flow-induced vibration problem has an additional parameter to take care of. As the structure moves, the boundary condition also changes and hence different discretization approaches such as immersed boundary (IB) method (Mittal and Iaccarino, 2005) can be employed. To solve the governing equation, Large Eddy Simulation (LES), Direct Numerical Simulation (DNS), or Reynolds-Averaged Navier-Stokes (RANS) have the capability to simulate on more realistic geometries but the complexity and

computational cost can be the barrier. The compromise between low computational cost and accuracy of the solution can be done by implementing reduced order models (ROMs) for EH designs.

3.1.2. Quasi-steady aerodynamics

Galloping is one particular example of a flow-induced vibration problem, where the characteristic time scale of the oscillation of the body is significantly greater than the characteristic timescale of the fluid flow. So, a quasi-steady hypothesis for the aerodynamic character of the flow can be justified. This assumption of quasi-steady approximation can be used by neglecting the unsteady terms.

3.1.3. Piezoelectricity

The electro-mechanical phenomenon in piezoelectric material occurs by the coupling of the electrical and mechanical states on the application of mechanical stress. The governing piezoelectric constitutive equation for direct and converse piezoelectric effects are given by

$$\begin{bmatrix} \delta \\ D \end{bmatrix} = \begin{bmatrix} S^E & s^t \\ d & \epsilon^T \end{bmatrix} \begin{bmatrix} \sigma \\ E \end{bmatrix} \qquad \text{Eq. 3.2}$$

(Erturk et al., 2011)

where, δ and σ are the strain and stress components, s, ε, and d are the elastic compliance, the dielectric constant, and the piezoelectric coefficient, respectively, D and E represent to the electric displacement and electric field components, the superscripts E and T represent the respective constants which are determined at the constant electric field and constant stress, respectively, and the superscript t is used for the transpose.

The Preprocessing and Post-processing are carried out using CAD/CAE tools. 3D CAD software and 3D CFD simulations are carried out as per the requirements.

Commercially available solvers including MATLAB, Fluent, and Mechanical APDL are used as the preferred research instrument in the current study.

Firstly, the geometric models of both fluid domain and the structural solid are created using SolidWorks 2016. Then, the mesh of the fluid domain is created using ANSYS ICEM and the structural mesh is generated by using ANSYS Meshing tool. The fluid domain mesh differs with the structural mesh with parameters such as mesh resolution and cell size. After that, the two computational meshes are imported to the respective numerical solvers (i.e. FLUENT and Transient Structural) in which the simulation setup is carried out. The solvers include the setup such as assigning properties of fluid and structure, allocating boundary conditions, setting the numerical schemes, etc. The structural model consists a square cylindrical member having elastic support and damping. Finally, System Coupling which exchanges the data is used to couple the two solvers in Workbench.

4.1. Geometry

The fluid domain is a rectangular prism in which the square cylindrical member of cross-section 40 mm X 40 mm is placed inside. Figure 4-1 shows the geometry of the entire fluid domain. The structural member is placed in the middle at a distance of 180 mm from the inlet of fluid domain. The horizontal and vertical dimension of the fluid domain is taken as 1200 mm and 600 mm respectively.

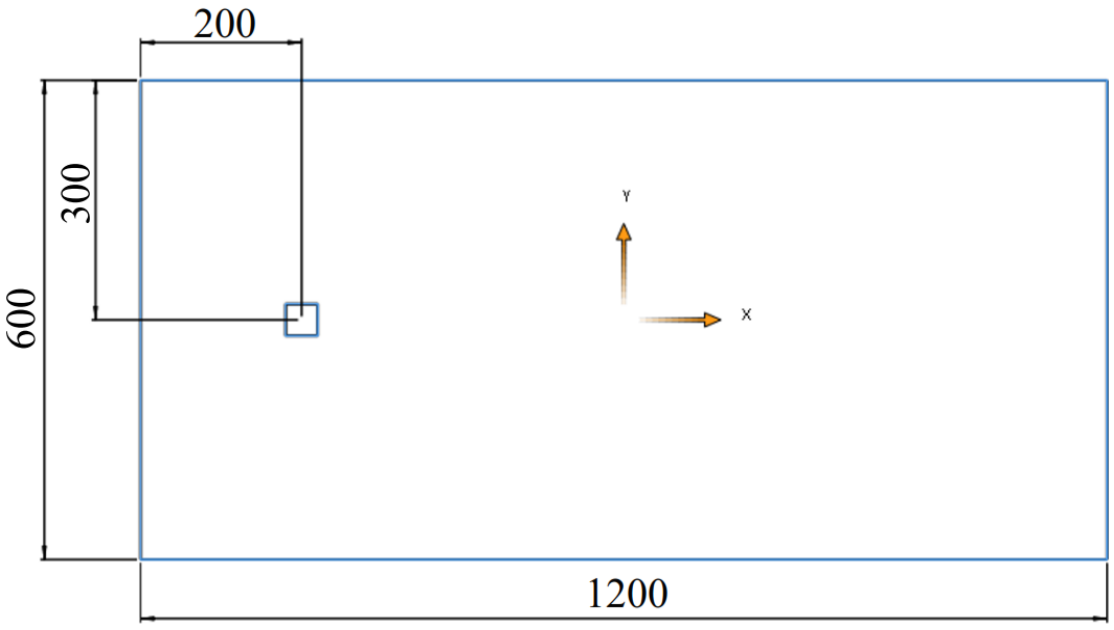

Units: mm

Figure 4-1: Geometry of fluid domain

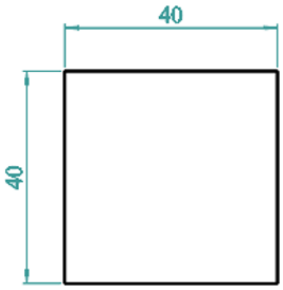

Figure 4-2: Structural Member

Figure 4-2 shows the geometry of the structural member. The position of the square cylindrical member in the transient structural model is same as that of the square wall in the fluid model which is assigned as a fluid-solid interface for transferring data between the two solvers.

4.2. Computational Mesh

ANSYS ICEM meshing tool is used for creating the computational mesh of the fluid domain. As the geometry is simple, the structured mesh is made up of quad cells. The total number of elements are 87,978. Figure 4-3 shows the entire computational fluid domain mesh.

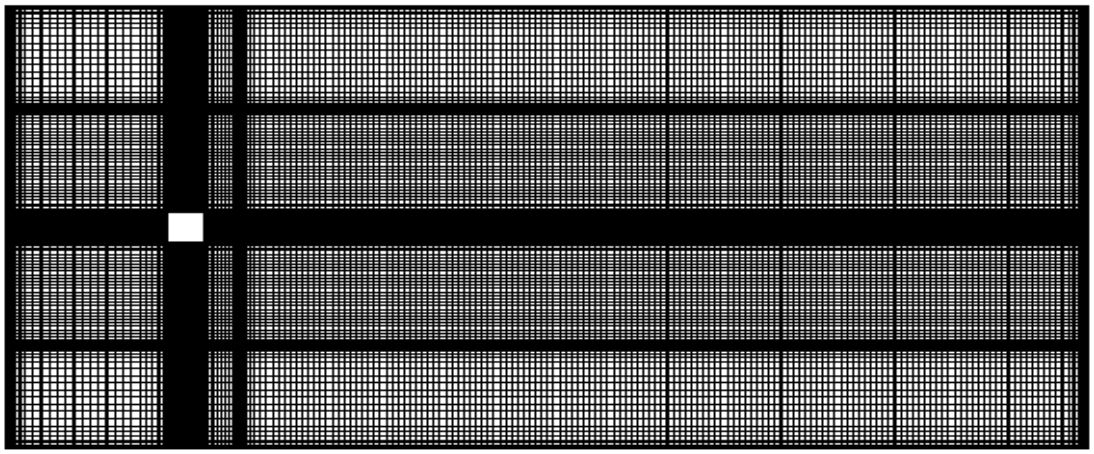

Figure 4-3: Computational mesh of the fluid domain

Generally, in CFD model special treatment is required for the boundary layers. For this, the non-dimensional distance from the wall to the first cell i.e. y^+ value is taken as an important parameter. Wall functions also play an important role when dealing with the flow near the wall region. Usually, y^+value in the limit 15- (100-1000) is considered depending on the turbulence model used (ANSYS Inc., 2013).

So, an initial cell height of ~1.3mm is estimated using y plus calculator. Thus, the first mesh layer is kept at 1.3mm height.

Figure 4-4 shows the computational mesh of the structural member which is created using ANSYS Meshing tool.

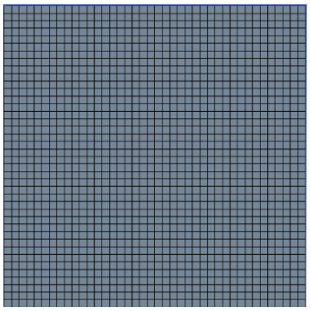

Figure 4-4: Structural mesh

The transient structural mesh consists of 1600 shell elements of Quad type.

4.3. Mesh Independence Test

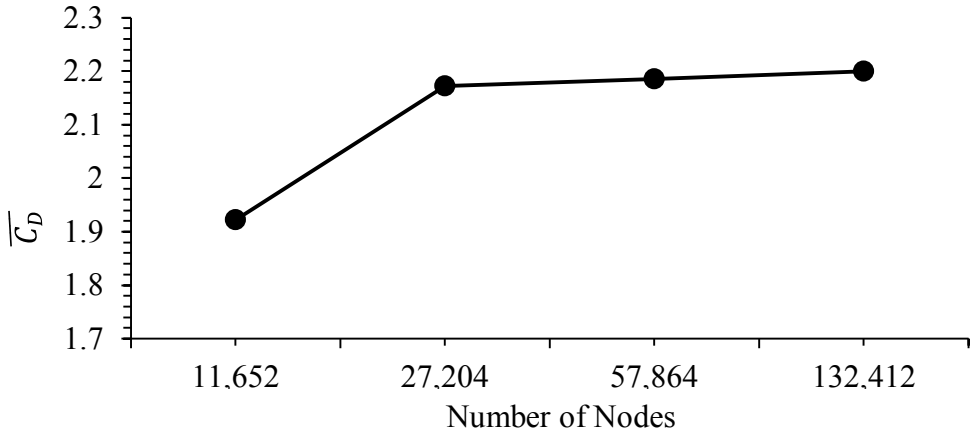

Figure 4-5: Spatial convergence of drag coefficient

Figure 4-5 is the mesh independence test which shows that a mesh element of 87,500 i.e., 57,000 nodes are sufficient to ensure accuracy of ± 0.006. With an increasing number of nodes from 11,652 to 27,204 the value of $\overline{C_D}$ increases drastically as the coarse mesh is not fine enough to capture all the flow features. So, the mesh density should be increased. After further increasing number of nodes from 57,000 the value of $\overline{C_D}$ doesn't change significantly ensuring it has reached mesh independence.

4.4. Different cases of Simulations

Firstly, the CFD analysis has been conducted under various Turbulence models. Section 2.4 explains about the turbulent flow and turbulence models. Table 4-1 shows the different turbulence models and the wall function considered for different cases.

Table 4-1: Turbulence Modeling Setup

Cases	Turbulence Models	Near Wall treatment
2D	Standard k-ϵ model	Standard wall function
2D	Realizable k-ϵ model	Standard wall function
2D	Smagorinsky - lilly sub grid scale LES model	-
2D with unit cell thickness	Standard k-ϵ model	Standard wall function

4.5. Simulation setup

Firstly, the setup of CFD model is carried out and then the structural model setup is carried out.

4.5.1. Material Properties

Gas (air) is used as fluid type in fluid model solver. Table 4-2 shows the key properties of air assigned in the setup.

Table 4-2: Material properties of air

Material	Density (kg/m^3)	Dynamic viscosity (kg/ms)
Air	1.225	$1.789 * 10^{-5}$

Table 4-3: Material properties of the structural member

Material	Density (kg/m^3)	Young's Modulus (GPa)	Poisson's ratio
Aluminum	2700	69	0.3

4.5.2. Turbulence Modeling Setup

The different turbulence models are used as per the various cases of simulations.

4.5.3. Cell Zone Condition

Fluid type (air) is assigned at the cell zone condition.

4.5.4. Boundary Conditions

Table 4-4 shows the boundary conditions assigned to the fluid model.

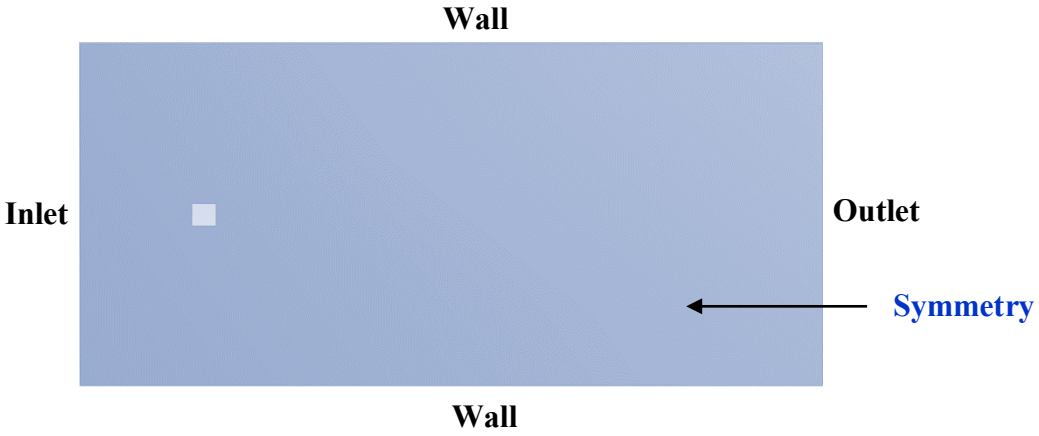

Figure 4-6: Boundary conditions of a fluid model

Table 4-4: Boundary conditions of a fluid model

Parts of the Domain	Type of boundary condition	Values
Inlet	Velocity - inlet	x-velocity = 12 m/s
Outlet	Pressure Outlet	Gauge pressure = 0 Pa
Tunnel wall side 1	Symmetry	-
Tunnel wall side 2	Symmetry	-
Tunnel wall top	Stationary wall	No slip
Tunnel wall bottom	Stationary wall	No slip
Square cylinder wall	Stationary wall	No slip
Int_fluid	Interior	-

Moreover, *dynamic mesh* settings should be added so as to induce a mesh deformation within the case of two- way coupling. In this part, the dynamic mesh zones are assigned to the boundaries of a fluid model. The Square cylinder wall is assigned to the *System Coupling* type, whereas, the symmetric boundaries are allotted to the *deforming* type.

4.5.5. Solver setup

Table 4-5 shows the discretization schemes (temporal and spatial) employed in Fluent.

Table 4-5: Discretization scheme used in Fluent

Temporal discretization	First-order implicit
Pressure-Velocity coupling	COUPLED
Step size	0.0001 sec
Spatial discretization	
Gradient	Least squares cell-based
Pressure	Second-order
Momentum	Second-order upwind
Turbulent kinetic energy (k)	First-order upwind
Turbulent dissipation rate (e)	First-order upwind

4.5.6. ANSYS Mechanical Setup

ANSYS Mechanical setup is simple in comparison to Fluent setup. Firstly, the geometry of the structural model is imported into the geometry setup of Transient Structural in Workbench. Then, Young's modulus and density of the structure are selected. The structural meshing is similar to the meshing performed in section 4.2. The ANSYS Mechanical setup includes assigning of the boundary conditions, loads, and analysis settings.

The bottom and top surface of the square cylinder are connected to elastic support of stiffness $100\ N/m$ and the surface of the cylinder is assigned as a fluid-solid interface upon which the calculated fluid forces are applied. Beside this, it has the identical transient setups as assigned in Fluent setup.

4.5.7. System Coupling Setup

This is a coupling tool which is used in Workbench for integrating fluid solver (such as FLUENT) and structural solver (such as Transient Structural) in multi-physics simulations. The procedure and working principle is explained in section 2.3.

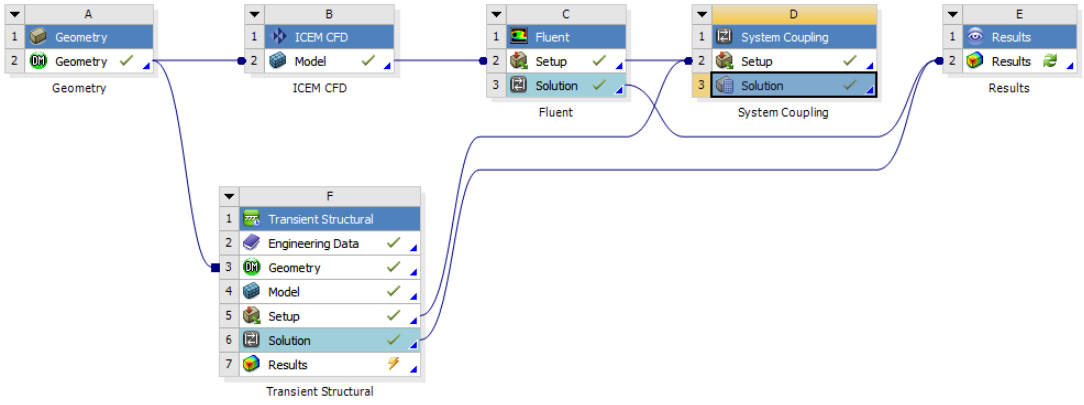

Figure 4-7: Workbench project schematic for FSI analysis

Figure (4-7) shows the project schematic of two-way FSI analysis using System coupling with Fluent solver and ANSYS mechanical solver. At first, the simulation setups of both the numerical solvers are completed, and then, the setup component of both the fluid and structural solvers are integrated into the setup component of System Coupling. Thus, the System Coupling identifies the fluid-structure interface and synchronizes the numerical conditions of both the solvers. Finally, the setup component of System Coupling is completed which comprises of following important steps.

- Analysis Settings: Time step size, end time, maximum and minimum number of coupling iteration should be provided in this setup.
- Data transfer: It is the foremost important step of the coupling setting which incorporates and directs the sequence of data transfer between the fluid and structural solvers. In two-way coupling analysis, data is transferred in the two directions i.e. first one from Fluent solver to ANSYS Mechanical solver (i.e. fluid forces) and at the same time, the second data (i.e. nodal displacements of structure) is transferred from ANSYS Mechanical solver to Fluent solver.
- Simulation sequence: In this, the working order of the respective solvers are assigned.

CHAPTER FIVE : RESULTS AND DISCUSSION

5.1. CFD Results of 2D with Unit Cell Thickness

Computational Fluid Dynamics (CFD) simulations of 2D geometry with unit cell thickness (Case IV) have been performed whose both sidewalls are assigned as symmetry in the boundary condition. Figure 5-1 shows the pressure contour variation with time. At the front side of the square, the stagnation point of the flow is located leading to an adverse pressure gradient in horizontal direction. Also, concurrently, flow separation starts from the upper side and the lower side of the structure. It has global minimum pressure of -190 Pa and a maximum pressure of 112.248 Pa. The pressure starts to decrease in a steady way towards the downstream.

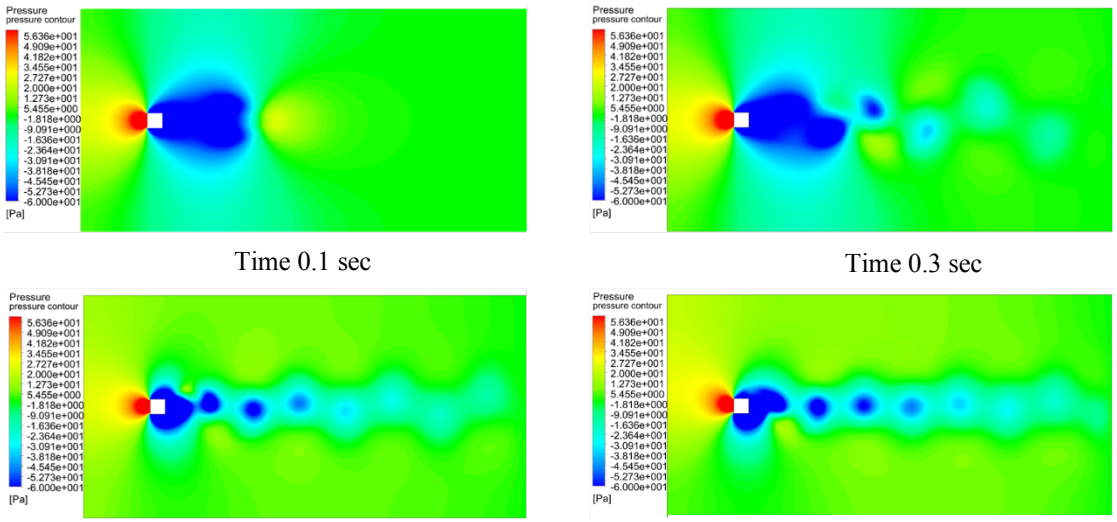

Time 0.1 sec

Time 0.3 sec

Time 0.5 sec

Periodic steady state contour at t = 3s

Figure 5-1: Pressure contour at different time-steps

Figure 5-2 shows the velocity contour variation at a different time step. The flow separation begins from the upper side and lower side of the structure and starts to oscillate in the wake region after 0.2 secs. In the region, just after the flow separation, maximum velocity of 19.17 m/s is attained.

Figure 5-3 shows the development of Von Karman Street with time. The vorticity field is developed due to the velocity in y-direction which is found to be 11.089 m/s in the negative y-direction and 11.091 m/s in the positive y-direction. The maximum and minimum vorticity z field is found to be $7600.4\ s^{-1}$ and $-5636.62\ s^{-1}$. The periodic vorticity field is in accordance with the vorticity field of Joly *et al.*, 2012.

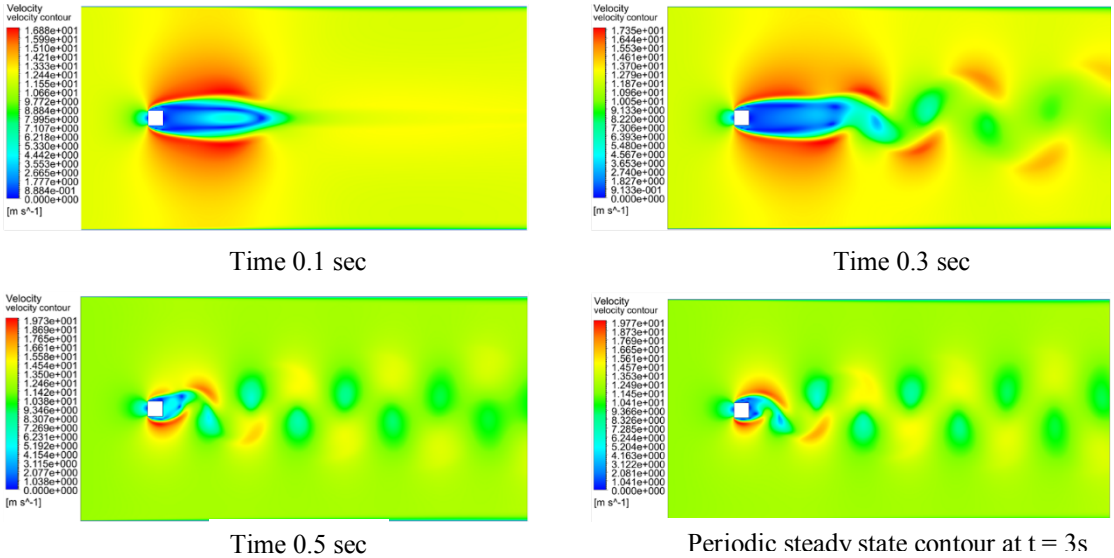

Figure 5-2: Velocity contour at different time-steps

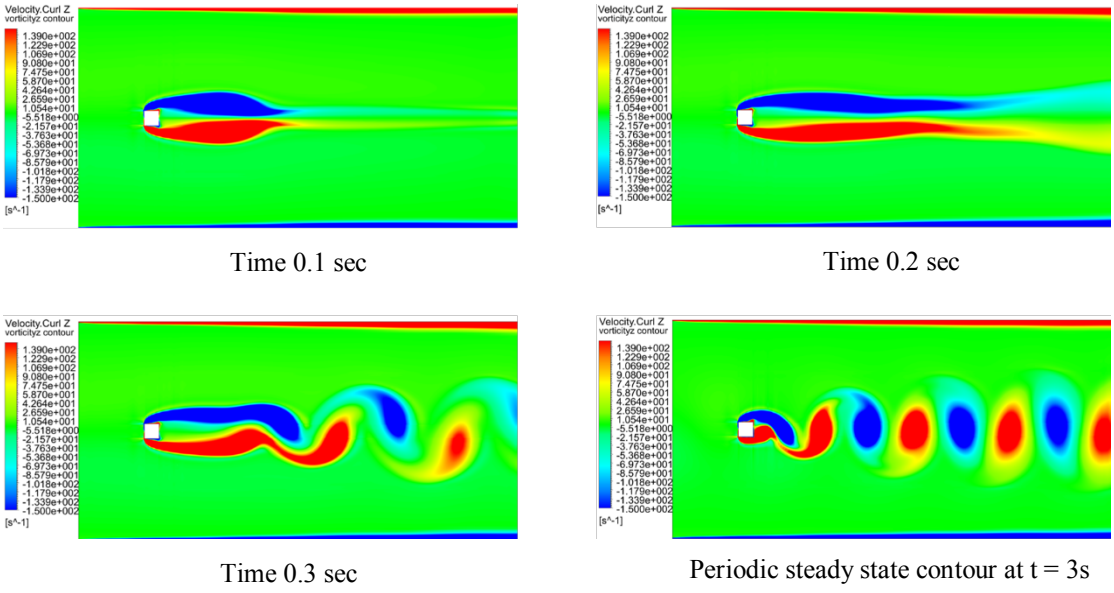

Figure 5-3: Vorticity Z contour at different time-steps

5.2. Drag and Lift Coefficient Vs Flow Time

Figure 5-4 to Figure 5-10 shows the lift and drag coefficient vs flow time at periodic steady-state of different cases. The mean drag coefficient is found to be 1.756 in case I and 2.024 in case II which agrees reasonably with the corresponding numerical data determined by (Franke and Rodi, 1993) and (Bosch and G., 1995)

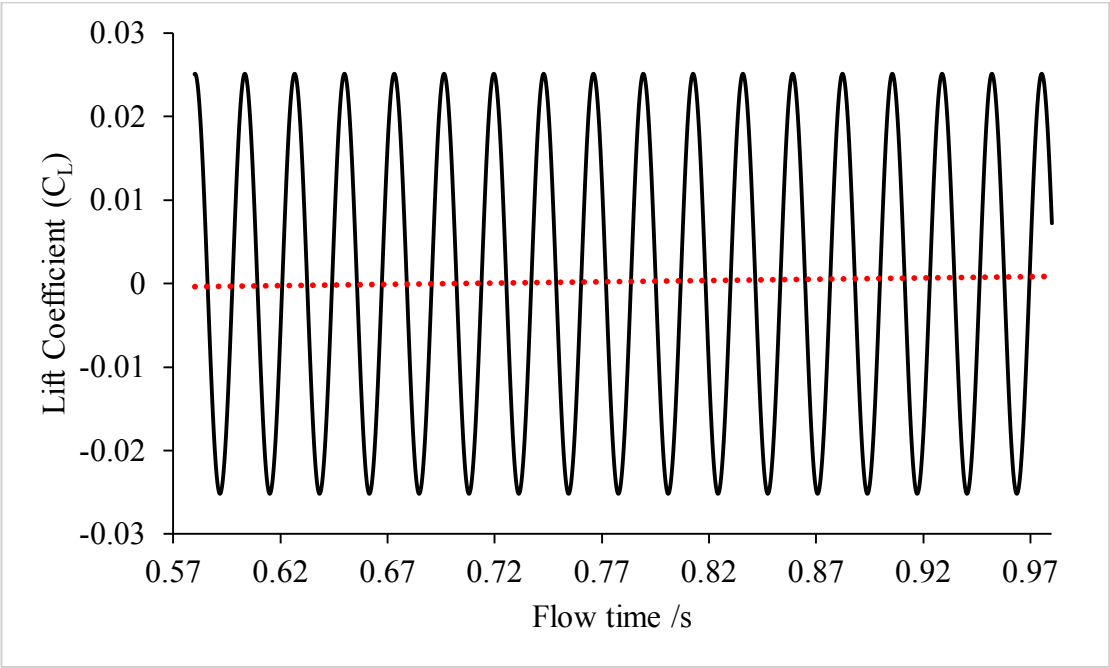

Figure 5-4: Lift coefficient vs Flow time of case I (SKE Model)

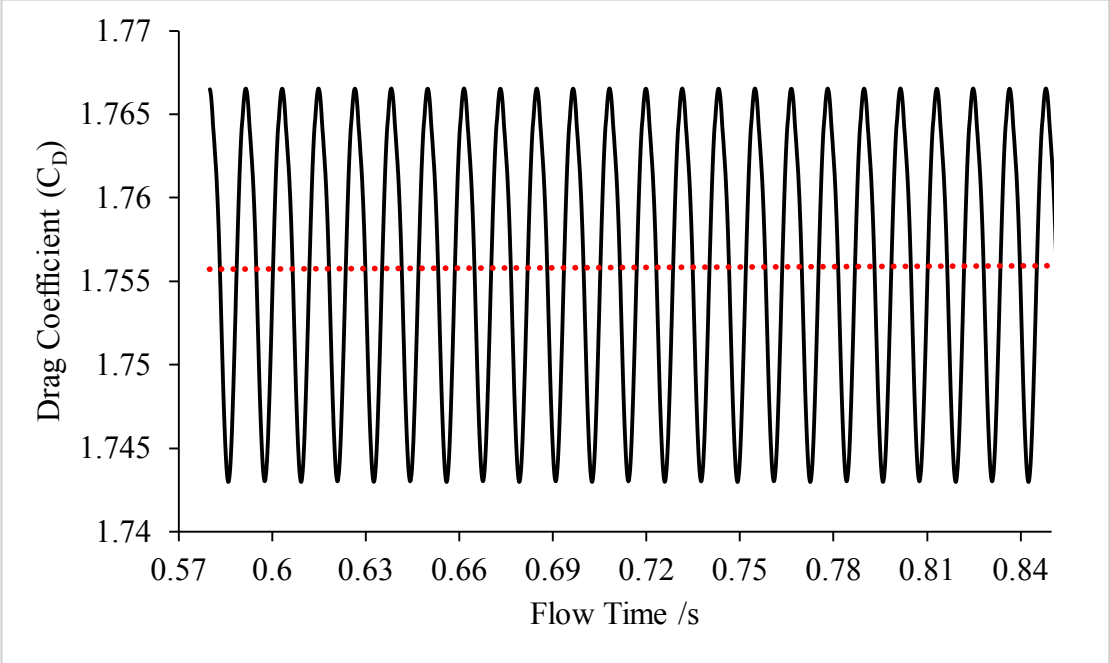

Figure 5-5 : Drag coefficient vs Flow time of case I (SKE Model)

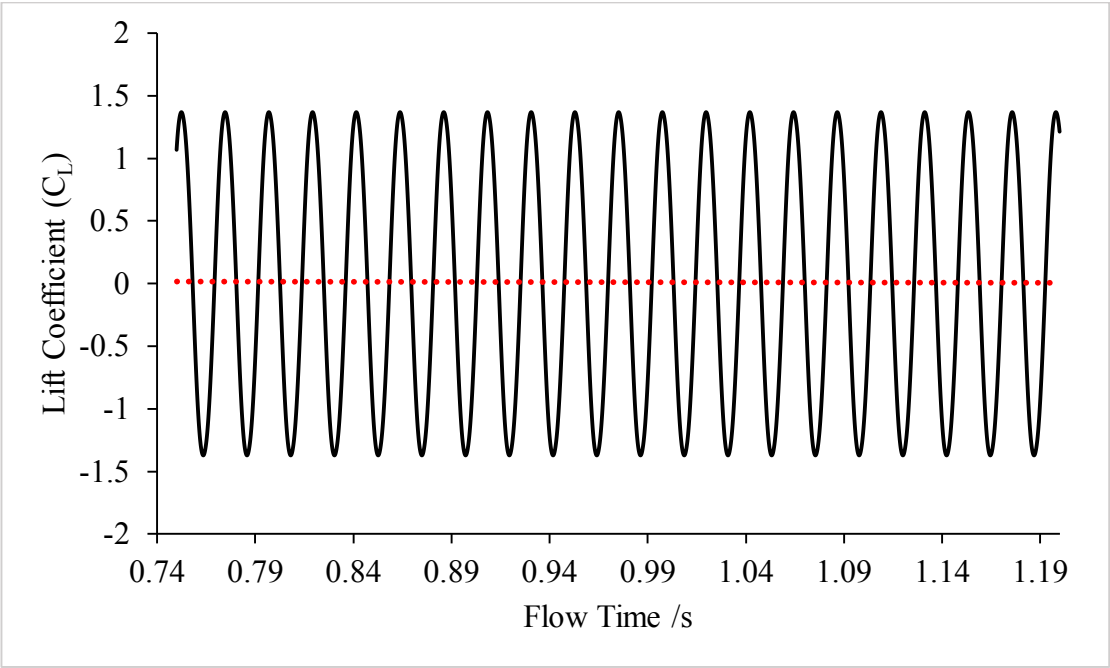

Figure 5-6: Lift coefficient vs Flow time of case II (RKE Model)

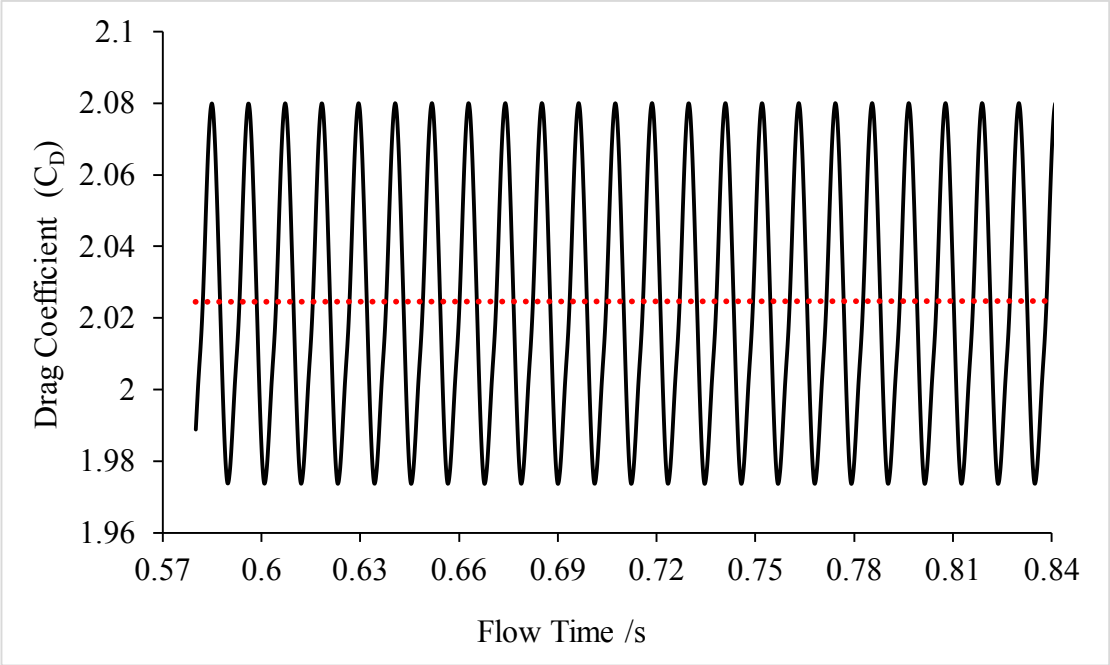

Figure 5-7: Drag coefficient vs Flow time of case II (RKE Model)

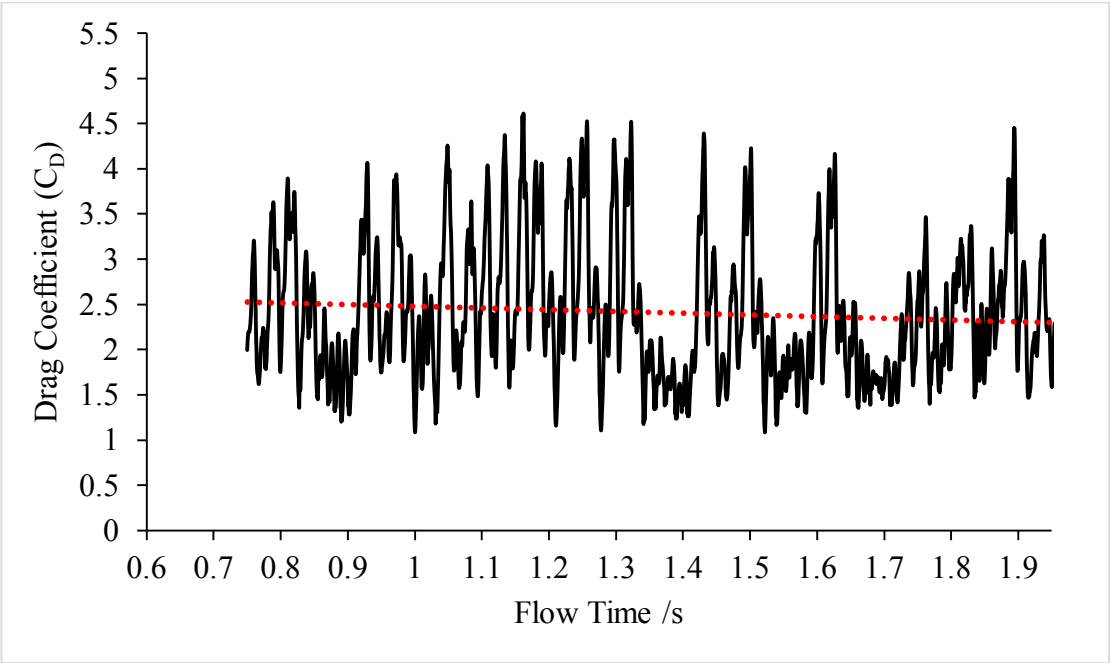

Figure 5-8: Drag coefficient vs Flow time of case III (LES Model)

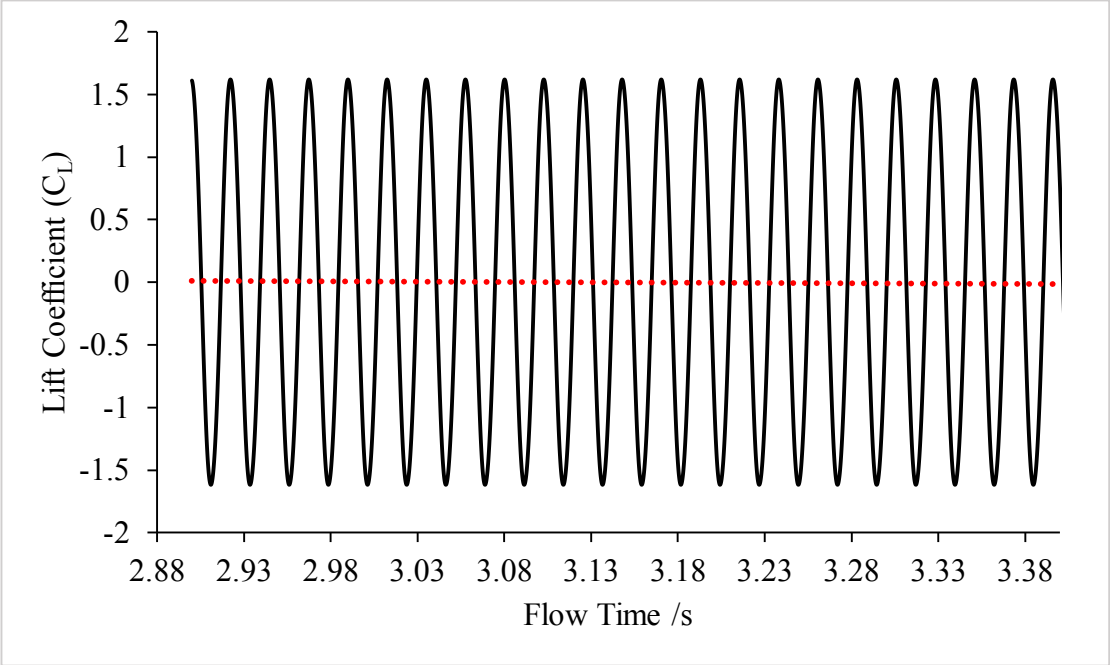

Figure 5-9: Lift coefficient vs Flow time of case IV (RKE Model)

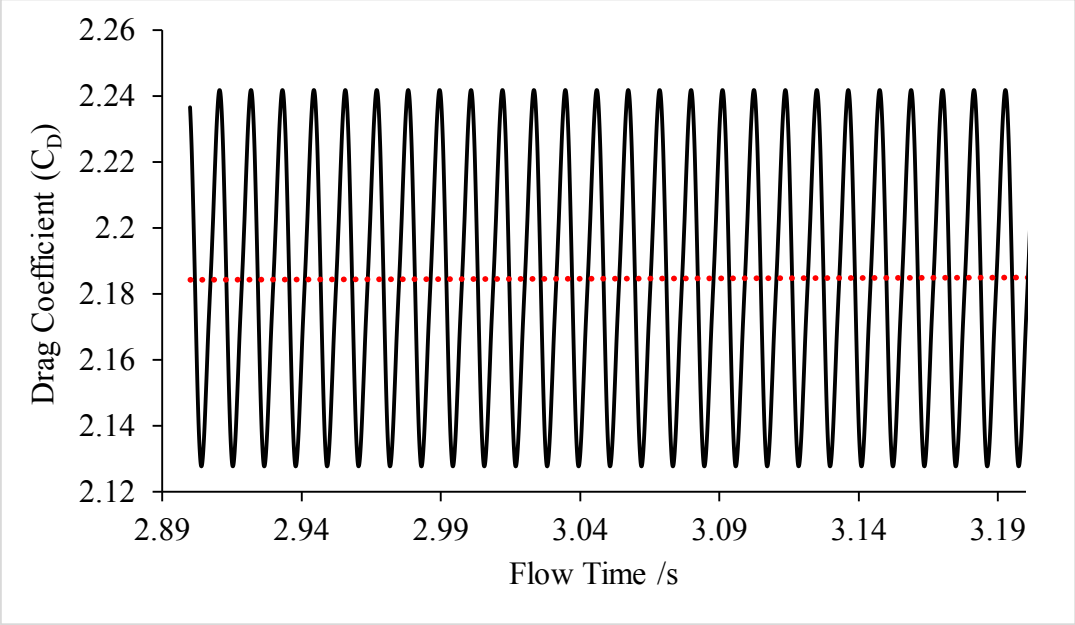

Figure 5-10: Drag coefficient vs Flow time of case IV (RKE Model)

Due to too large pressure and too long separation region, in case I, the value of C_D is low (Rodi, 1995). Case III (LES model) requires larger computational time to reach periodic steady state, however, the LES model yielded the mean C_D value of 2.4. And in Case IV mean coefficient of drag is found to be 2.185 which agrees reasonably with the corresponding numerical data.

5.3. Fluid-Structure Interaction (FSI) Results

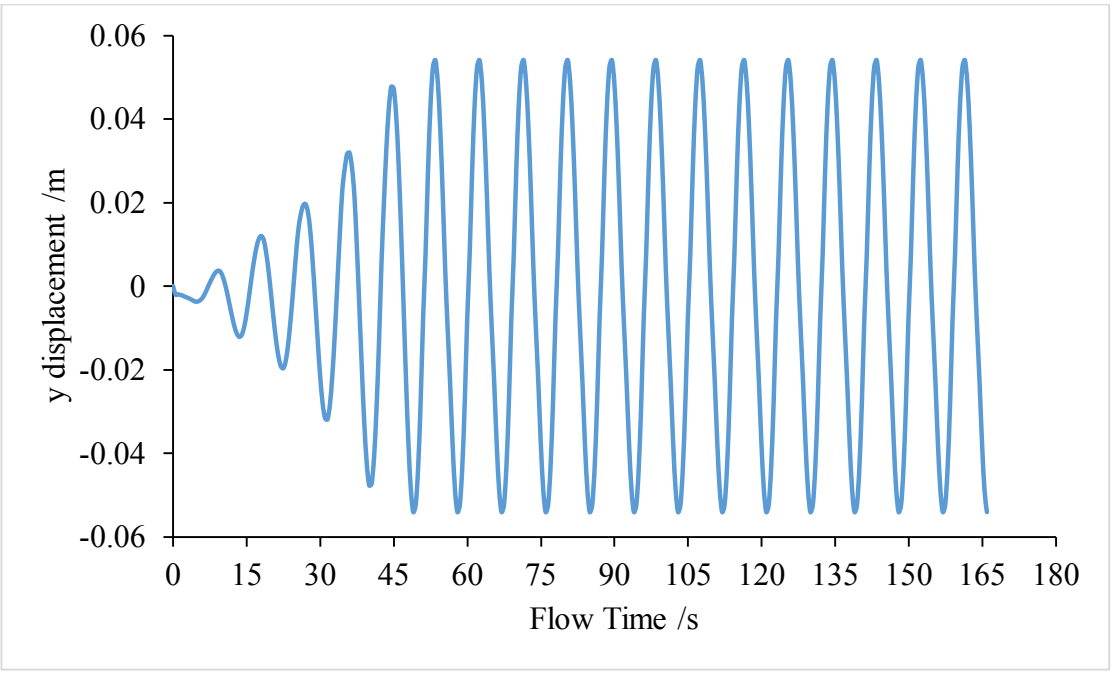

Figure 5-11: Tip displacement Vs Flow time

Two-way FSI simulations of 2D geometry with unit cell thickness have been performed to predict the tip displacement attached to the cantilever beam. Figure 5-11 shows the predicted tip displacement whose amplitude gradually increases with time and finally reaches a steady value. The maximum amplitude predicted is approximately $50.4\ mm$ which is considerable for the beam of length $170\ mm$.

Two PZT-5A type piezoelectric sheets having electromechanical coupling term $\theta = 1.55\ mN/V$ and the equivalent capacitance of $C_p = 120\ nF$ (Erturk *et al.*, 2010) are used in the analysis to predict the voltage generated due to tip displacement.

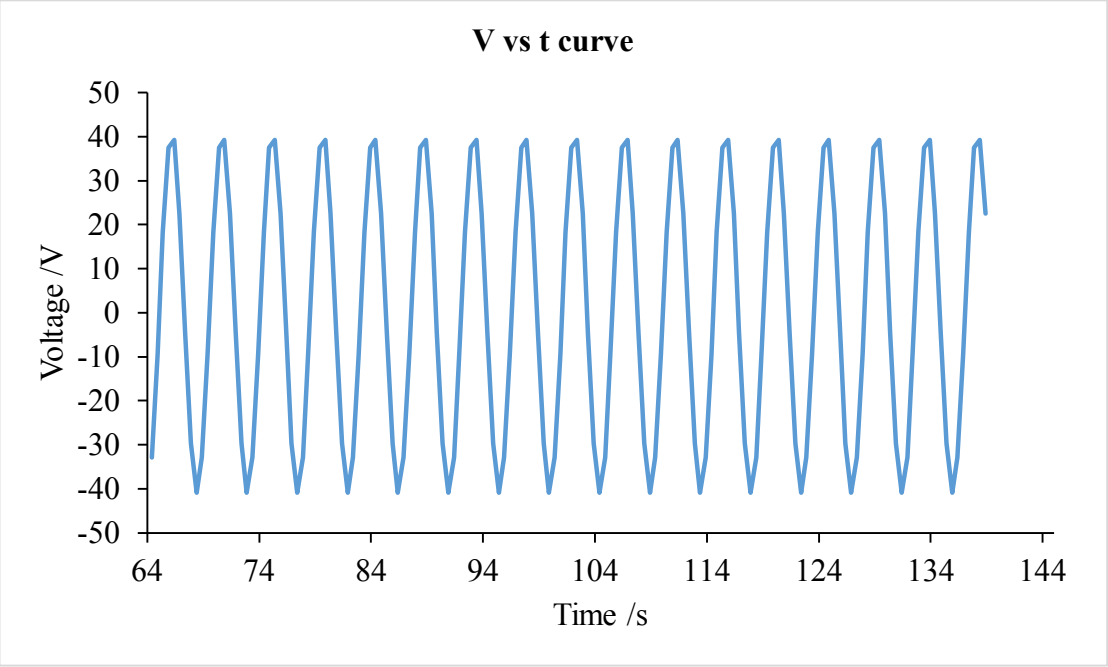

Figure 5-12: Steady Voltage generated by piezoelectric sheets at 0.7 MΩ load resistance

The output voltage predicted by solving Equation (2.11) at a wind velocity of $12\ m/s$ and across a load resistance of $0.7\ M\Omega$ at a steady state is shown in Figure 5-12. The maximum steady-state voltage of $38\ V$ is predicted and the peak output power ($P = V_{peak}^2/R_L$), where V_{peak} is the peak Voltage across load resistance (R_L) is found to be $2.1\ mW$.

5.4. Validation and Comparison of Results

Table 5-1: Comparison of global parameters

Reference		Re ($x10^3$)	$\overline{C_L}$	$\overline{C_D}$	Strouhal Number (St)
Numerical Results					
LES Model	(Verstappen and Veldman, 1997)	22.0	0.005	2.09	0.133
	(Pourquie et al., 1997)	22.0	-0.02	2.2	0.13
	(Wang and Vanka, 1997)	22.0	0.04	2.03	0.13
	(Kawashima and Kawamura, 1997)	22.0	0.01	2.72	0.16
SKE Model	(Bosch and G., 1995)	22.0	-	1.64	0.134
Experimental Results					
(Lyn et al., 1995), (Lyn, 1994)		22.0	-	2.1	0.132
(Luo, S.C. et al., 1994)		34.0		2.21	0.13-0.14
Case I (SKE Model)		33.0	0.001	1.756	0.141
Case II (RKE Model)		33.0	-0.025	2.024	0.142
Case III (LES Model)		33.0	-	2.4	-
Case IV (RKE Model) (2D with unit cell thickness)		33.0	-0.035	2.185	0.1428

Table 5-1 summarizes the different global parameters which are calculated by averaging the last 20 steady vortex shedding cycles of the simulations for comparison such as the dimensionless shedding frequency (Strouhal number $St = f\frac{D}{U}$), where, f is the vortex shedding frequency, the mean drag coefficient (C_D), and the mean lift coefficient (C_L) at Reynolds number ($Re = \rho UD/\mu$) 22,000 to 34,000.

The vortex shedding frequency (f) is determined by FFT analysis to calculate the Strouhal number. The Strouhal number (St) obtained is slightly greater than the experimental data which may be due to differences in boundary conditions mostly wall law or may be due to differences in damping functions used. However, they have a similar accuracy with the corresponding numerical results.

Also, the predicted steady-state voltage in Figure 5-12 is in close agreement with that of Sirohi and Mahadik, 2012.

CHAPTER SIX : CONCLUSIONS AND RECOMMENDATIONS

6.1. Conclusions

In this research, a theoretical spring supported damped model coupled to a purely resistive energy harvesting circuit representing the dynamics of the transverse motion of a system has been considered. Based on the CFD and FSI simulations results, the following major points can be concluded.

- Different turbulence models are analyzed for the CFD simulations of which Realizable k-ϵ model yielded the most accurate solution. So, this model has been considered for the FSI simulation.
- This study has illustrated the numerical investigation of aeroelastic energy harvesting based on the galloping phenomenon at a wind velocity of $12\ m/s$ and a load resistance of $0.7\ M\Omega$ across piezoelectric sheets.
- The CFD simulation results are validated with the corresponding numerical and experimental data and the tip displacement result having maximum amplitude $50.4\ mm$ obtained from FSI simulation is used to predict the amount of energy that could be harvested.
- A maximum steady-state voltage of $38\ V$ and a peak output power of $2.1\ mW$ is predicted that can be used to power small sensors.
- Damping ratio of 0.001 is accounted for the geometric nonlinearities of piezoelectric material in structural solver.

6.2. Recommendations

The recommendations for continuing this work in the future have been summarized in the points below.

- Although the quasi-steady approximation is considered in the research, proper development of unsteady flow representation is required for higher velocities.
- A parametric study is recommended for improvement of the harvested power from the galloping phenomenon by analyzing the effects of the mechanical parameters and the electrical load resistance across piezoelectric.
- Also, an experimental study is recommended for validation and improvement of research.

REFERENCES

Abdelkefi, A. (2016) 'Aeroelastic energy harvesting: A review', *International Journal of Engineering Science*. Elsevier Ltd, 100, pp. 112–135. doi: 10.1016/j.ijengsci.2015.10.006.

Abdelkefi, A., Hajj, M. R. and Nayfeh, A. H. (2013) 'Piezoelectric energy harvesting from transverse galloping of bluff bodies', *Smart Materials and Structures*, 22(1). doi: 10.1088/0964-1726/22/1/015014.

Abdelkefi, A., Nayfeh, A. H. and Hajj, M. R. (2012) 'Modeling and analysis of piezoaeroelastic energy harvesters', *Nonlinear Dynamics*, 67(2), pp. 925–939. doi: 10.1007/s11071-011-0035-1.

Abdelkefi, A., Yan, Z. and Hajj, M. R. (2013) 'Modeling and nonlinear analysis of piezoelectric energy harvesting from transverse galloping', *Smart Materials and Structures*, 22(2). doi: 10.1088/0964-1726/22/2/025016.

Akaydin, H. D. et al. (2010) 'Wake of a cylinder: A paradigm for energy harvesting with piezoelectric materials', *Experiments in Fluids, 49*, 291–304.

Akaydin, H. D. et al. (2012) 'The performance of a self-excited fluidic energy harvester', *Smart Materials and Structures, 21*, 025007.

ANSYS Inc. (2013) 'Workbench User's Guide', *ANSYS Manual*, 15317(Release 15.0), pp. 724–746.

ANSYS Inc (2013) 'ANSYS Fluent Theory Guide', *ANSYS Inc., USA*, 15317(November), pp. 724–746.

Barrero-Gil, A., Alonso, G. and Sanz-Andres, A. (2010) 'Energy harvesting from transverse galloping', *Journal of Sound and Vibration*. Elsevier, 329(14), pp. 2873–2883. doi: 10.1016/j.jsv.2010.01.028.

Benra, F. K. *et al.* (2011) 'A comparison of one-way and two-way coupling methods for numerical analysis of fluid-structure interactions', *Journal of Applied Mathematics*, 2011. doi: 10.1155/2011/853560.

Bibo, A., Abdelkefi, A. and Daqaq, M. F. (2015) 'Modeling and characterization of a piezoelectric energy harvester under combined aerodynamic and base excitations',

Journal of Vibration and Acoustics, Transactions of the ASME, 137(3), pp. 1–12. doi: 10.1115/1.4029611.

Blevins, R. D. (2001) *Flow-Induced Vibration*.

Bosch and G. (1995) 'Experimentelle und theoretische Untersuchung der instationaren Stromung um zylindrische Strukturen', *University of karlsruhe*.

Bryant, M., Wolff, E., & Garcia, E. (2011). Aeroelastic flutter energy harvester design: The sensitivity of the driving instability to system parameters. *Smart Materials and Structures, 20*, 125017.

Elahi, H., Eugeni, M. and Gaudenzi, P. (2018) 'A review on mechanisms for piezoelectric-based energy harvesters', *Energies*, 11(7). doi: 10.3390/en11071850.

Erturk, A. *et al.* (2010) 'On the energy harvesting potential of piezoaeroelastic systems', *Applied Physics Letters*, 96(18). doi: 10.1063/1.3427405.

Erturk, A. and Inman, D.J. (2011) '*Piezoelectric energy harvesting'*. John Wiley & Sons.

Joly, A., Etienne, S. and Pelletier, D. (2012) 'Galloping of square cylinders in cross-flow at low Reynolds numbers', *Journal of Fluids and Structures*. Elsevier, 28, pp. 232–243. doi: 10.1016/j.jfluidstructs.2011.12.004.

Den Hartog, J.P. (1956) 'Mechanical Vibrations', New York: Mcgrraw Hill Nook Company.

Kawashima, N. and Kawamura, H. (1997) 'Numerical Analysis of Les of Flow Past a Long Square Cylinder', in, pp. 413–422. doi: 10.1007/978-94-011-5624-0_40.

Luo, S.C., Yazdani, M.G., Chew, Y.T. and Lee, T.S. (1994) 'Effects of incidence and afterbody shape on flow past bluff cylinders', *Journal of wind engineering and industrial aerodynamics*, *53*(3), pp.375-399. https://doi.org/10.1016/0167-6105(94)90092-2.

Lyn, D. A. et al. (1995) 'A laser-Doppler velocimetry study of ensemble-averaged characteristics of the turbulent near wake of a square cylinder', *Journal of Fluid Mechanics*.

Lyn, D. et al. (1994)) 'The flapping shear layer formed by flow separation from the forward corner of a square cylinder', *cambridge.org*.

Mittal, R. and Iaccarino, G. (2005) 'Immersed Boundary Methods', *Annu. Rev. Fluid Mech*, 37, pp. 239–61. doi: 10.1146/annurev.fluid.37.061903.175743.

Ochoa, J.S. and Fueyo, N. (2004) 'Large Eddy Simulation of the flow past a square cylinder', In *Proceedings of the PHOENICS 10th International User Conference, Melbourne, Australia* (pp. 3-5).

Païdoussis, M.P., Price, S.J. and De Langre, E. (2010) '*Fluid-structure interactions: cross-flow-induced instabilities*', Cambridge University Press.

Pourquie, M., Breuer, M. and Rodi, W. (1997) 'Computed Test Case: Square Cylinder', in, pp. 375–379. doi: 10.1007/978-94-011-5624-0_34.

Raja, R. S. (2012) 'Coupled fluid structure interaction analysis on a cylinder exposed to ocean wave loading', *Chalmers University of Technology*.

Rodi, W. (1995) 'Simulation of Flow Past Buildings with Statistical Turbulence Models', in *Wind Climate in Cities*. Springer Netherlands, pp. 649–668. doi: 10.1007/978-94-017-3686-2_31.

Sirohi, J. and Mahadik, R. (2011) 'Piezoelectric wind energy harvester for low-power sensors', *Journal of Intelligent Material Systems and Structures*, 22(18), pp. 2215–2228. doi: 10.1177/1045389X11428366.

Sirohi, J. and Mahadik, R. (2012) 'Harvesting wind energy using a galloping piezoelectric beam', *Journal of Vibration and Acoustics, Transactions of the ASME*, 134(1), pp. 1–8. doi: 10.1115/1.4004674.

Smagorinsky, J. (1963) 'General Circulation Experiments With The Primitive Equations', *Monthly Weather Review*. American Meteorological Society, 91(3), pp. 99–164. doi: 10.1175/1520-0493(1963)091

Verstappen, R. W. C. P. and Veldman, A. E. P. (1997) 'Fourth-Order DNS of Flow Past a Square Cylinder: First Results', in, pp. 381–384. doi: 10.1007/978-94-011-5624-0_35.

Wang, G. and Vanka, S. P. (1997) 'Les of Flow Over a Square Cylinder', in. Springer, Dordrecht, pp. 397–400. doi: 10.1007/978-94-011-5624-0_37.

Yang, Y., Zhao, L. and Tang, L. (2013) 'Comparative study of tip cross-sections for efficient galloping energy harvesting', *Applied Physics Letters*, 102(6). doi: 10.1063/1.4792737.

Zhao, L., Tang, L. and Yang, Y. (2013) 'Comparison of modeling methods and parametric study for a piezoelectric wind energy harvester', *Smart Materials and Structures*, 22(12). doi: 10.1088/0964-1726/22/12/125003.

http://www.cfd-online.com/Tools/yplus.php

PUBLICATION

Thakur, S., Darlami, K. and Poudel, L., (2020) 'Aeroelastic Energy Harvesting: A Case for Galloping', Lalitpur, IOE Graduate Conference.

APPENDIX A : CFD 2D RESULTS

Case I (Standard k- ϵ Model)

Figure A-1 shows the pressure contour variation with time. It has global minimum pressure of -166.022 Pa and a maximum pressure of 104.237 Pa. At the front side of the square, the stagnation point of the flow is located and there is an adverse pressure difference in the horizontal direction as the flow starts to separate from the upper side and lower side of the structure. The pressure starts to decrease in a steady way towards the downstream.

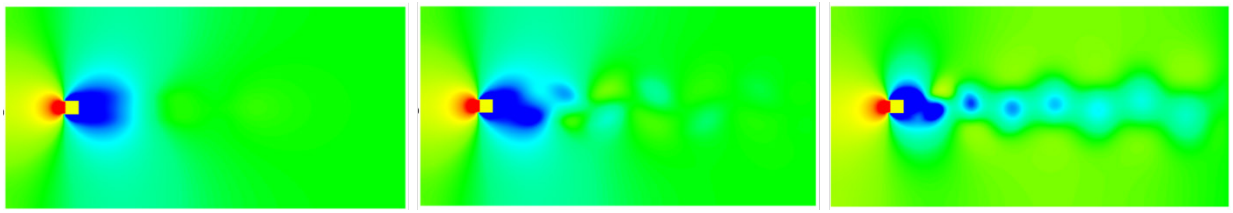

Time 0.1 sec Time 0.2 sec Time 0.3 sec

Figure A- 1:Pressure Contour of SKE Model at time step 0.1, 0.2 and 0.3 sec

Figure A-2 shows the velocity contour at a different time step. The flow separates from the upper and lower side of the structure and starts to oscillate in the wake region after 0.2 secs. In the region, just after the flow separation, maximum velocity of 18.2 m/s is attained.

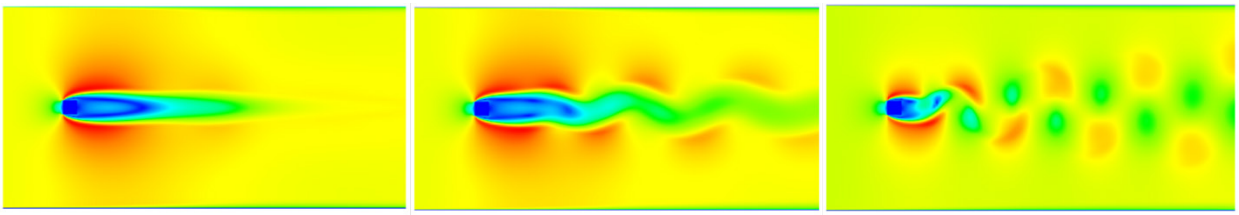

Time 0.1 sec Time 0.2 sec Time 0.3 sec

Figure A- 2: Velocity Contour of SKE Model at time step 0.1, 0.2 and 0.3 sec

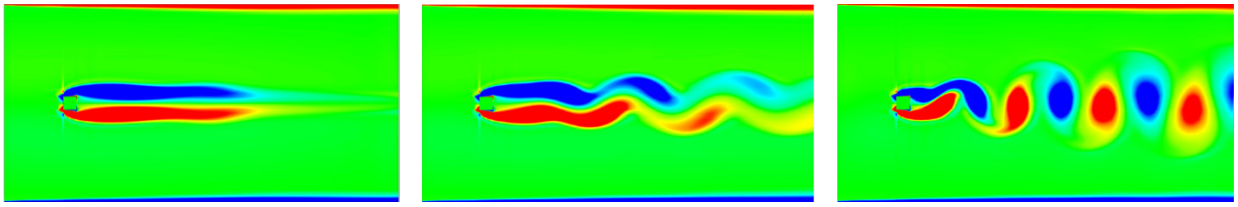

Time 0.1 sec Time 0.2 sec Time 0.3 sec

Figure A- 3: Development of Vortex sheet of SKE Model at 0.1, 0.2 and 0.3 sec

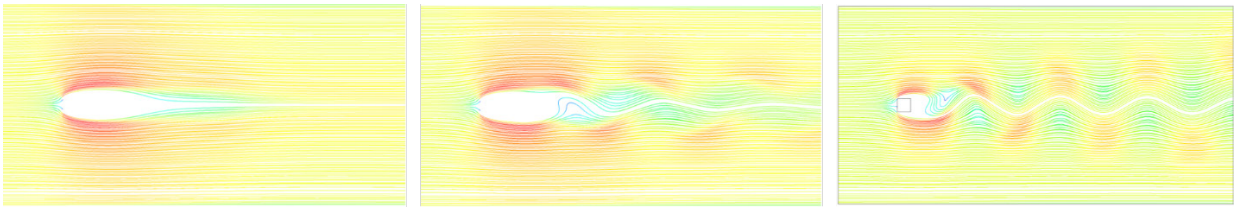

Time 0.1 sec Time 0.2 sec Time 0.3 sec

Figure A- 4: Velocity streamline of SKE Model at 0.1, 0.2 and 0.3 sec

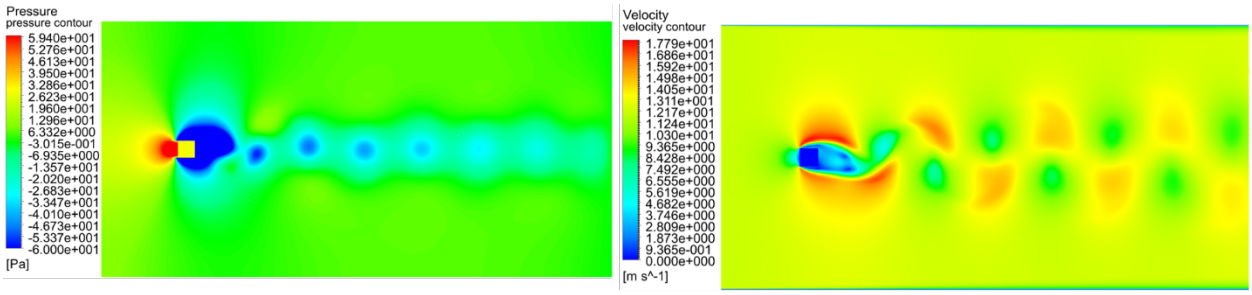

Pressure Contour Velocity Contour

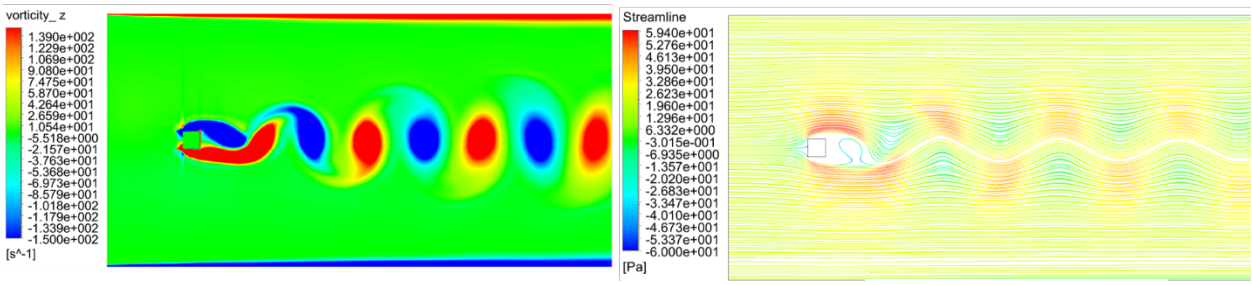

Vorticity Z Contour Velocity Streamline

Figure A- 5: Periodic steady state contours of SKE Model at 1.7 sec

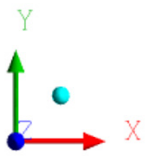

Figure A-3 shows the development of Von Karman Street with time. The vorticity field is developed due to the velocity in y-direction which is found to be 11.089 m/s in the negative y-direction and 11.091 m/s in the positive y-direction. The maximum and minimum vorticity z field is found to be 5830.5 s^{-1} and -6057.18 s^{-1} at time 1.7 sec. Figure A-5 shows the periodic steady-state contours which start to occur after 1.3 secs.

Case II (Realizable k - ϵ Model)

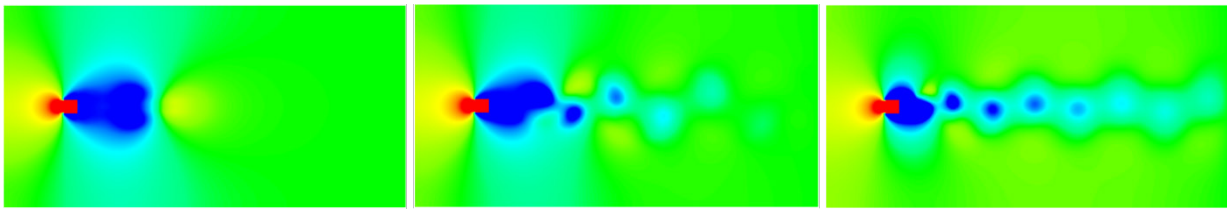

Time 0.1 sec Time 0.2 sec Time 0.3 sec

Figure A- 6: Pressure contour of RKE Model at 0.1, 0.2 and 0.3 sec

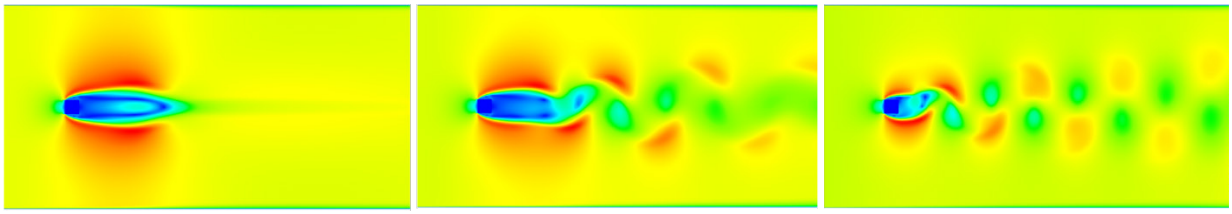

Time 0.1 sec Time 0.2 sec Time 0.3 sec

Figure A- 7: Velocity contour of RKE Model at 0.1, 0.2 and 0.3 sec

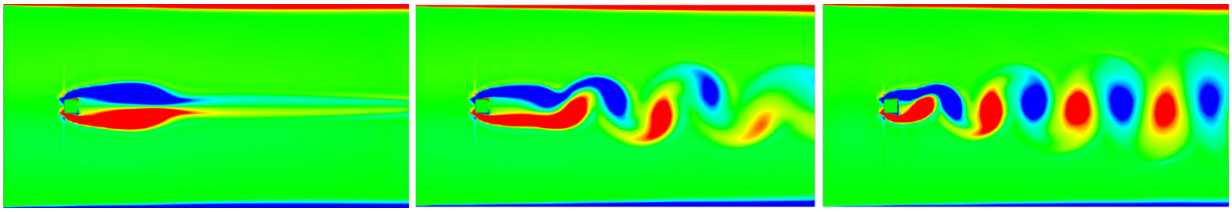

Time 0.1 sec Time 0.2 sec Time 0.3 sec

Figure A- 8: Development of Vortex sheet of RKE Model at 0.1, 0.2 and 0.3 sec

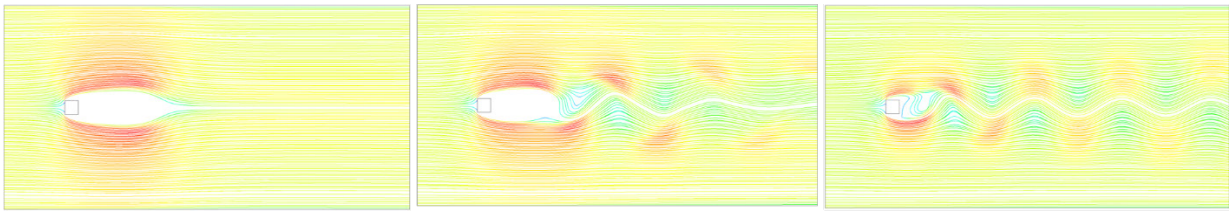

Time 0.1 sec Time 0.2 sec Time 0.3 sec

Figure A- 9: Velocity streamline of RKE Model at 0.1, 0.2 and 0.3 sec

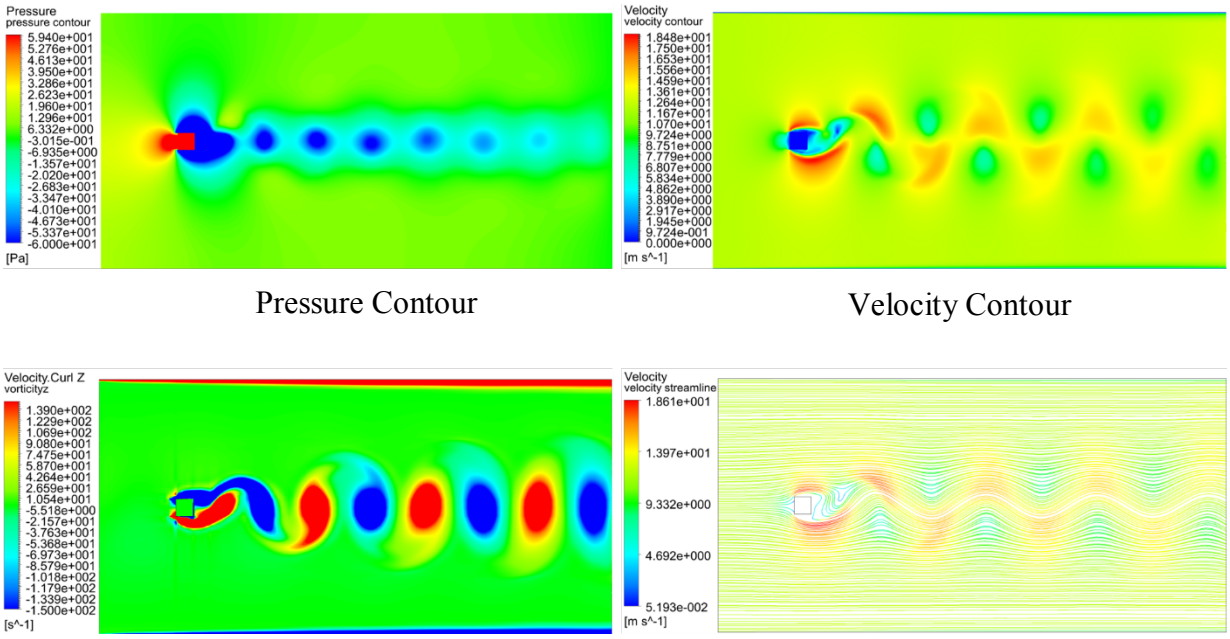

Pressure Contour

Velocity Contour

Figure A- 10: Periodic steady state contours of RKE Model at 1.7 sec

Vorticity Z Contour

Velocity Streamline

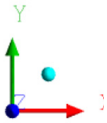

The results of Realizable k - ϵ model shows near about the same pattern as that of Standard k - ϵ model. In this, the periodic steady flow occurs after 0.4 secs. The maximum and minimum pressure is found to be 105.682 Pa and -218.569 Pa respectively. Here, the minimum pressure is lower than that of SKE model. The maximum velocity of 19.5 m/s is attained just after the point of flow separation. The minimum and maximum vorticity z field is found to be -6729.71 s^{-1} and 5583.83 s^{-1} respectively. The global y-velocity is found to be 11.916 m/s in the negative y-direction and 11.86 m/s in positive y-direction due to which the vortex sheet is developed in the wake region.

Case III (Smagorinsky-lilly LES Model)

The result obtained in this case is better than the case I since this model captures the smaller eddies which other cases were unable to model it. But this model requires large computational time to reach periodic steady-state due to which it would be computationally more expensive.

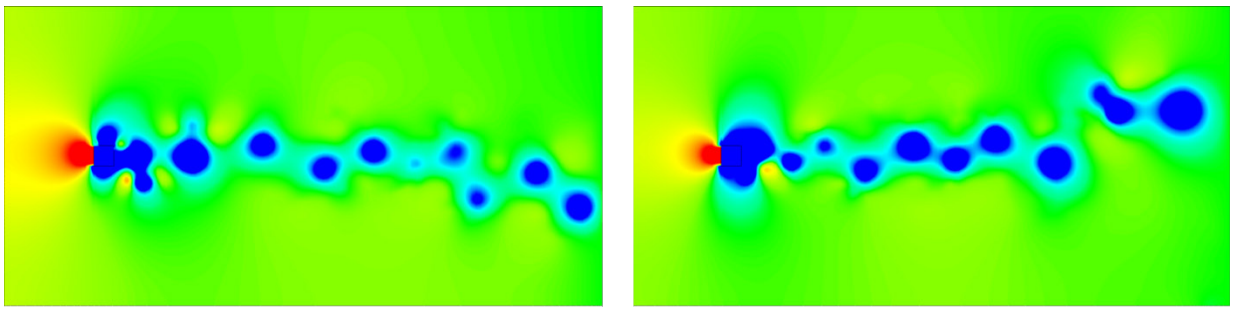

Time 9.2 sec Time 9.4 sec

Figure A- 11: Pressure contour of LES Model at 9.2 and 9.4 sec

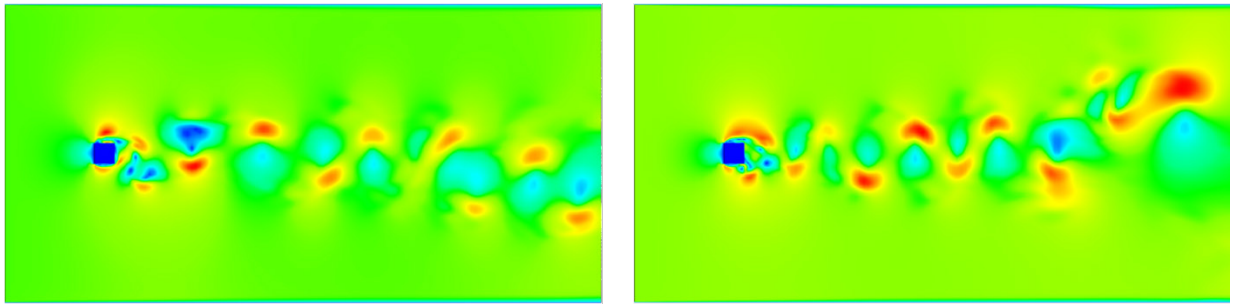

Time 9.2 sec Time 9.4 sec

Figure A- 12: Velocity contour of LES Model at 9.2 and 9.4 sec

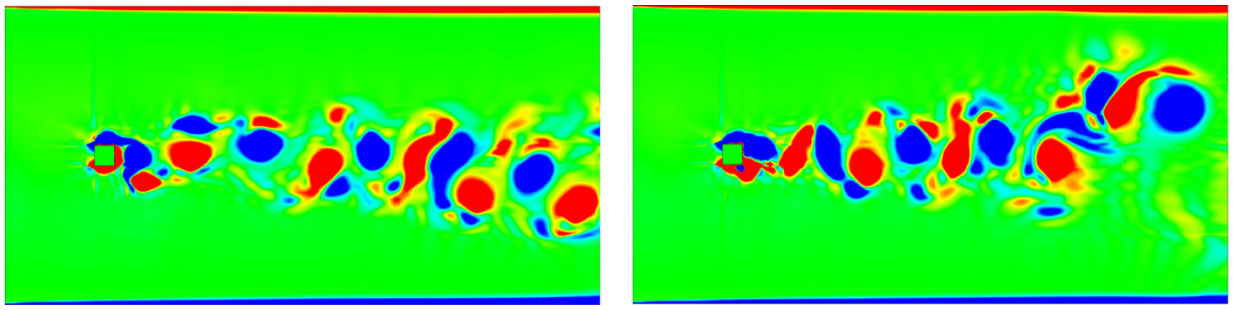

Time 9.2 sec Time 9.4 sec

Figure A- 13: Vorticity Z contour of LES Model at 9.2 and 9.4 sec

The global minimum and maximum pressure, in this case, is found to be -398.375 Pa and 114.657 Pa. The minimum is found to be much lower than the case I and case II. The minimum and maximum vorticity z field is found to be -5857.29 s^{-1} and 6552.65 s^{-1} respectively at time 9.4 secs. The global y-velocity is found to be 15.1 m/s in the negative y-direction and 12.85 m/s in the positive y-direction.

APPENDIX B : MATLAB CODES

Voltage Generated by Piezoelectric Sheets at Steady State

```
clear
syms V(t) y(t)

 Cp = 120e-9        % Equivalent Capacitance of Piezoelectric
 RL = 0.7e6         % Load Resistance across electrical circuit
 theta = 1.55e-3    % Electromechanical Coupling Term
 A = 0.05041          % Amplitude of y displacement

 y(t) = A*sin(0.698131*t)
ode = (diff(V,t))*Cp + V/RL + theta*diff(y,t) == 0;
cond = V(0) == 0;     %  Initial Condition
Vsol(t) = dsolve(ode,cond)
t = [50:150];

plot(t,Vsol(t), 'b')     %Plot of voltage generated at steady state
title('V vs t curve')
xlabel('Time/s')
ylabel('Voltage/V')
```

APPENDIX C : PYTHON CODE FOR CALCULATION OF STROUHAL NUMBER

```
import numpy as np
import scipy.signal as signal
import matplotlib.pyplot as plt

# # Loading Results
data = np.loadtxt('cl.txt')

L       = 0.04          # length of square body(m)
V       = 12        # Flow Velocity(m/s)
time    = data[:,0]
Cl      = data[:,1]

del data

# # Computing FFT Analysis
N       = len(time)
dt      = time[2] - time[1]

# # FFT
nmax=  2800   # no. of points in the fft
# freq, Cd_amp = signal.welch(Cd, 1./dt, nperseg=nmax)
freq, Cl_amp = signal.welch(Cl, 1./dt, nperseg=nmax)
plt.plot(freq, Cl_amp)
plt.show()

# # Strouhal Number Calculation
# Finding  the index corresponding to max amplitude
Cl_max_fft_idx = np.argmax(abs(Cl_amp))
freq_shed      = freq[Cl_max_fft_idx ]
St             = freq_shed * L / V
print('Vortex shedding frequency: %f [Hz]' %(freq_shed))
print('Strouhal Number: %f' %(St))
```